The Astrophysical Journal, 678:1005–1031, 2008 May 10

THE c2d *SPITZER* SPECTROSCOPIC SURVEY OF ICES AROUND LOW-MASS YOUNG STELLAR OBJECTS. II. CO_2

Klaus M. Pontoppidan,[1,2] A. C. A. Boogert,[3] Helen J. Fraser,[4] Ewine F. van Dishoeck,[5] Geoffrey A. Blake,[1] Fred Lahuis,[5] Karin I. Öberg,[5] Neal J. Evans II,[6] and Colette Salyk[1]

Received 2007 September 25; accepted 2007 November 28

ABSTRACT

This paper presents *Spitzer* IRS $\lambda/\Delta\lambda \sim 600$ spectroscopy of the CO_2 15.2 μm bending mode toward 50 embedded young low-mass stars, taken mostly from the "Cores to Disks" (c2d) Legacy program. The average abundance of solid CO_2 relative to water in low-mass protostellar envelopes is 0.32 ± 0.02, significantly higher than that found in quiescent molecular clouds and in massive star-forming regions. A decomposition of the observed CO_2 bending mode profiles requires a minimum of five unique components. Roughly $\frac{2}{3}$ of the CO_2 ice is found in a water-rich environment, while most of the remaining $\frac{1}{3}$ is found in a CO environment with strongly varying relative concentrations of CO_2 to CO along each line of sight. Ground-based observations of solid CO toward a large subset of the c2d sample are used to further constrain the CO_2:CO component and suggest a model in which low-density clouds form the CO_2:H_2O component and higher density clouds form the CO_2:CO ice during and after the freezeout of gas-phase CO. The abundance of the CO_2:CO component is consistent with cosmic-ray processing of the CO-rich part of the ice mantles, although a more quiescent formation mechanism is not ruled out. It is suggested that the subsequent evolution of the CO_2 and CO profiles toward low-mass protostars, in particular the splitting of the CO_2 bending mode due to pure, crystalline CO_2, is first caused by distillation of the CO_2:CO component through evaporation of CO due to thermal processing to ~20–30 K. The formation of pure CO_2 via segregation from the H_2O rich mantle may contribute to the band splitting at higher levels of thermal processing ($\gtrsim$50 K) but is harder to reconcile with the physical structure of protostellar envelopes around low-luminosity objects.

Subject headings: astrochemistry — circumstellar matter — dust, extinction — ISM: evolution

1. INTRODUCTION

Although CO_2 is not an abundant gas-phase molecule in molecular clouds, it is one of a small number of molecular species consistently found in very high abundances inside ice mantles on dust grains ($>10^{-5}$ with respect to H_2; Gerakines et al. 1999; Whittet et al. 2007). The generally high abundance of solid CO_2 became apparent with the spectroscopic surveys conducted with the *Infrared Space Observatory* (*ISO*; Gerakines et al. 1999; Nummelin et al. 2001). Other species known to belong to this class of very abundant molecules are CO and H_2O. In less than 10% of dark cloud regions surveyed, methanol (CH_3OH) is also found with similar abundances (Pontoppidan et al. 2003a; Boogert et al. 2008, hereafter Paper I). Depending on the density and temperature of a cloud, the CO is found partly in the gas phase and partly frozen onto grain surfaces, while the CO_2 and H_2O are completely frozen as ice mantles (Bergin et al. 1995), except in very hot or shocked regions (Boonman et al. 2003; Nomura & Millar 2004; Lahuis et al. 2007). The system of CO, CO_2, H_2O, and, under some conditions, CH_3OH therefore represents the bulk of solid-state volatiles in dense star-forming clouds, and interactions between these four species can be expected to account for most of the solid-state observables. Other species with abundances of less than 5% relative to water, such as CH_4, NH_3, OCN^-, HCOOH, and OCS, will be good tracers of chemistry and their local molecular environment but are unlikely to strongly affect the molecular environments, and therefore the band profiles, of the four major species.

The formation mechanism of solid CO_2 in the cold interstellar medium is still not understood, although a number of plausible scenarios have been proposed. Since the direct surface route, $CO + O \rightarrow CO_2$, is thought to possess a significant activation barrier, it was initially suggested that strong UV irradiation was needed to produce the observed CO_2 ice (d'Hendecourt et al. 1985). Laboratory simulations of interstellar ice mixtures of H_2O and CO confirmed that CO_2 is indeed readily formed during strong UV photolysis (d'Hendecourt et al. 1986), and initial detection of abundant CO_2 ice around UV-luminous massive young stars seemed to confirm this picture. However, recent detections of similar abundances of CO_2 in dark clouds observed along lines of sight toward background stars, far away from any ionizing source (Bergin et al. 2005; Knez et al. 2005; Whittet et al. 2007), argue against a UV irradiation route to CO_2, at least through enhanced UV from nearby protostars. Pontoppidan (2006) showed evidence for an increasing abundance of CO_2 ice with gas density in at least one low-mass star-forming core. Furthermore, the original premise of a barrier to oxygenation of CO is now in doubt (Roser et al. 2001). Consequently, both theoretical and laboratory efforts to understand the formation of CO_2 are still very active.

Extensive surveys of the 3.1 and 4.67 μm stretching mode of H_2O and CO ices have been carried out in a range of different star-forming environments (Whittet et al. 1988; Chiar et al. 1995; Pontoppidan et al. 2003b). However, CO_2 can only be observed from space, and surveys have until recently been limited

[1] California Institute of Technology, Division of Geological and Planetary Sciences, Pasadena, CA 91125; pontoppi@gps.caltech.edu.
[2] Hubble Fellow.
[3] IPAC, NASA Herschel Science Center, California Institute of Technology, Pasadena, CA 91125.
[4] Department of Physics, Scottish Universities Physics Alliance (SUPA), University of Strathclyde, Glasgow G4 ONG, UK.
[5] Leiden Observatory, NL-2300 RA Leiden, Netherlands.
[6] Department of Astronomy, University of Texas at Austin, Austin, TX 78712-0259.

to a small sample of very luminous young stars (Gerakines et al. 1999). While the 4.27 μm stretching mode of CO_2 was detected toward a few background field stars by *ISO* (Whittet et al. 1998; Nummelin et al. 2001), recent *Spitzer* observations of the 15.2 μm bending mode of CO_2 have extended the sample of CO_2 along quiescent lines of sight considerably (Knez et al. 2005; Bergin et al. 2005; Whittet et al. 2007).

The profiles of the CO_2 ice bands observed in quiescent regions and along lines of sight toward luminous protostars show intriguing differences. In particular, ice in massive star-forming regions, which presumably traces more processed material, tends to show a splitting of the 15.2 μm bending mode. This splitting has been identified as a general property of crystalline pure CO_2 and is readily reproduced in laboratory simulations of interstellar ices (e.g., Ehrenfreund et al. 1997; van Broekhuizen et al. 2006). It seems implausible that this pure CO_2 layer would form directly through gas-phase deposition and subsequent surface reactions, and it has been suggested that the CO_2 segregates from a $CO_2:H_2O:CH_3OH = 1:1:1$ mixture on strong heating (Gerakines et al. 1999). Annealing in a laboratory setting produces the same effect (Ehrenfreund et al. 1997), and strong heating is not unreasonable in the envelopes of massive young stars with luminosities in excess of $10^3\ L_\odot$.

In this paper, a survey of the 15.2 μm CO_2 bending mode toward ~50 young *low-mass* stars using the high-resolution mode of the Infrared Spectrograph (IRS) on board the *Spitzer Space Telescope* is presented. The sample stars have typical luminosities in the range 0.1–10 $L_\odot$, thus bridging the observational gap between the background stars and the massive protostars from the *ISO* sample. The *Spitzer* spectra are complemented by ground-based observations of H_2O and CO ices, where available, as well as the archival spectra from *ISO* used in Gerakines et al. (1999). While this paper concentrates on the region around 15 μm, Paper I discusses the ices causing the 5–8 μm absorption complex. The 7.7 μm CH_4 and 9.0 μm NH_3 bands are described in two separate papers (Öberg et al. 2008 and S. Bottinelli et al. 2008, in preparation, respectively).

The central questions that are addressed using the new *Spitzer* spectra of the CO_2 bending mode are as follows:

1. What are the differences, if any, between CO_2 ice in massive and low-mass star-forming environments?
2. What is the average abundance of CO_2 in low-mass protostellar envelopes compared to lower density quiescent clouds?
3. In which molecular environments can solid CO_2 be found, and what are their relative abundances?
4. Which process forms CO_2 in CO-dominated environments when the CO accretes from the gas phase at high densities?
5. How does the component of pure CO_2 (as measured by the well-known splitting of the bending mode) form in low-mass protostellar envelopes?
6. What is the evolution of the CO_2 ice and what does it tell us about protostellar evolution?

2. THE INFRARED BANDS OF SOLID CO_2

The infrared vibrational modes of CO_2 are known to be very sensitive to the molecular environment. Observations of the band profiles can determine whether the CO_2 molecules are embedded with water, CO, and other CO_2 molecules. Solid CO_2 has two strong vibrational modes: the asymmetric stretching mode centered on 4.27 μm, and the bending mode at 15.2 μm. The stretching mode is so strong that it is typically saturated along lines of sight through protostellar envelopes, and its $^{13}CO_2$ counterpart at 4.38 μm is often used for profile analysis instead. However, neither stretching mode is covered by the spectral range of *Spitzer* IRS.

Fortunately, the CO_2 bending mode is an excellent diagnostic of molecular environments. For instance, pure CO_2 will typically produce a split band in the bending mode due to Davydov splitting, a long range interaction in crystalline materials. Conversely, CO_2 embedded in a hydrogen-bonding matrix will produce a broad, smooth profile. While these differences are relatively well known, it is noted that the different formation scenarios from gas-grain chemical models make distinct predictions for the molecular environment of the CO_2. Thus, models favoring a formation route via OH predict that the CO_2 will be found in a water-dominated matrix.

Indeed, observations of the CO_2 stretching and bending modes toward young massive stars with *ISO* (Gerakines et al. 1999) have shown that the CO_2 ice is dominated by a band consistent with CO_2 in a hydrogen-bonding environment. They also found that a double-peaked component, consistent with a relatively pure, crystalline CO_2, is generally present at a lower level toward their sample of massive stars.

3. OBSERVATIONS

The spectra of the 15.2 μm CO_2 bending mode have been obtained using the Short-High (SH) module of *Spitzer* IRS, with a spectral resolving power of $\lambda/\Delta\lambda \sim 600$, covering 10–19.5 μm, corresponding to 1 cm^{-1}. The *Spitzer* spectra were obtained as part of the "Cores to Disks" Legacy program (PIDs 172 and 179), as well as a few archival spectra observed as part of the GTO programs (PID 2). All SH spectra from the c2d database that show clear detections of the CO_2 bending mode have been included. The spectra have been reduced using the c2d pipeline from basic calibrated data (BCD) products version S13.0.2. For each spectrum, clearly deviant points were removed and individual orders were scaled by small factors to align the overlapping regions between orders. The overlapping regions between these two orders usually match very well, which lends support to the reality of small features in the spectra for most sources. A small number of sources show evidence for absorption by the Q-branch of gas-phase CO_2 at 15.0 μm. Since this survey is concerned with solid CO_2, pixels affected by gas-phase absorption have been removed from the fits of IRS 46, WL 12, and DG Tau B. Some of the most embedded sources have saturated or nearly saturated bending mode bands. For these sources, special care has to be taken to ensure that the background level is well determined.

In addition to the *Spitzer* data, the five highest quality spectra of massive YSOs observed with the *ISO* SWS (Gerakines et al. 1999) have been included. The *ISO* spectra provide a useful comparison of the structure of CO_2 ices in the warmer, more energetic envelopes of young massive stars to the comparatively quiescent envelopes of low-mass YSOs.

Finally, to study the relation of the CO_2 ices with CO and water, ground-based spectra of the 4.67 μm stretching mode of solid CO and the 3.08 μm stretching mode of water ice have been collected using the Infrared Spectrometer and Array Camera (ISAAC) on the Very Large Telescope (VLT).[7] Most of the 4.67 μm VLT ISAAC spectra are published in Pontoppidan et al. (2003b), but a significant fraction are previously unpublished spectra obtained with NIRSPEC at the Keck Telescope. Sources with no CO ice data are typically too faint for useful ground-based 4.67 μm spectroscopy. The column densities of water ice

[7] Based on observations made with ESO Telescopes at the Paranal Observatory under program ID 164.C-0605.

TABLE 1

OBSERVED SAMPLE OF EMBEDDED YOUNG STARS

Source	CO_2	CO and H_2O	R.A. (J2000.0)	Decl. (J2000.0)	ObsID
W3 IRS 5	*ISO* SWS	NIRSPEC	02 25 40.8	+62 05 52.8	42701302
L1448 IRS 1	*Spitzer*	NIRSPEC	03 25 09.4	+30 46 21.7	5656832
L1448 NA	*Spitzer*	...	03 25 36.5	+30 45 21.4	5828096
L1455 SMM 1	*Spitzer*	...	03 27 43.2	+30 12 28.8	15917056
RNO 15	*Spitzer*	NIRSPEC	03 27 47.7	+30 12 04.3	5633280
IRAS 03254+3050	*Spitzer*	NIRSPEC	03 28 34.5	+31 00 51.2	13460480
IRAS 03271+3013	*Spitzer*	NIRSPEC	03 30 15.2	+30 23 48.8	5634304
B1-a	*Spitzer*	NIRSPEC	03 33 16.7	+31 07 55.1	15918080
B1-c	*Spitzer*	...	03 33 17.9	+31 09 31.0	15916544
IRAS 03439+3233	*Spitzer*	NIRSPEC	03 47 05.4	+32 43 08.5	5635072
IRAS 03445+3242	*Spitzer*	NIRSPEC	03 47 41.6	+32 51 43.8	5635328
L1489 IRS	*Spitzer*	ISAAC	04 04 43.1	+26 18 56.4	3528960
DG Tau B	*Spitzer*	NIRSPEC	04 27 02.7	+26 05 30.5	3540992
GL 989	*ISO* SWS	NIRSPEC	06 41 10.2	+09 29 33.7	72602619
HH 46 IR	*Spitzer*	ISAAC	08 25 43.8	−51 00 35.6	7130112
CED 110 IRS 4	*Spitzer*	...	11 06 46.6	−77 22 32.4	5639680
CED 110 IRS 6	*Spitzer*	ISAAC	11 07 09.2	−77 23 04.3	5639680
B35	*Spitzer*	...	11 07 21.5	−77 22 11.8	5639680
IRAS 12553−7651	*Spitzer*	...	12 59 06.6	−77 07 40.0	9830912
ISO ChaII 54	*Spitzer*	...	13 00 59.2	−77 14 02.7	15735040
IRAS 13546−3941	*Spitzer*	...	13 57 38.9	−39 56 00.2	5642752
IRAS 15398−3359	*Spitzer*	...	15 43 02.3	−34 09 06.7	5828864
GSS 30 IRS 1	*Spitzer*	ISAAC	16 26 21.4	−24 23 04.1	5647616
WL 12	*Spitzer*	ISAAC	16 26 44.2	−24 34 48.4	5647616
GY 224	*Spitzer*	NIRSPEC	16 27 11.2	−24 40 46.7	9829888
WL 20	*Spitzer*	...	16 27 15.7	−24 38 45.6	9829888
IRS 37	*Spitzer*	ISAAC	16 27 17.6	−24 28 56.5	5647616
IRS 42	*Spitzer*	ISAAC	16 27 21.5	−24 41 43.1	5647616
WL 6	*Spitzer*	ISAAC	16 27 21.8	−24 29 53.3	5647616
CRBR 2422.8−3423	*Spitzer*	ISAAC	16 27 24.6	−24 41 03.3	9346048
IRS 43	*Spitzer*	ISAAC	16 27 27.0	−24 40 52.0	12699648
IRS 44	*Spitzer*	ISAAC	16 27 28.1	−24 39 35.0	12699648
Elias 32/IRS 45	*Spitzer*	ISAAC	16 27 28.4	−24 27 21.4	12664320
IRS 46	*Spitzer*	ISAAC	16 27 29.4	−24 39 16.3	9829888
VSSG 17/IRS 47	*Spitzer*	ISAAC	16 27 30.2	−24 27 43.4	5647616
IRS 51	*Spitzer*	ISAAC	16 27 39.8	−24 43 15.1	9829888
IRS 63	*Spitzer*	ISAAC	16 31 35.7	−24 01 29.5	9827840
L1689 IRS 5	*Spitzer*	...	16 31 52.1	−24 56 15.2	12664064
RNO 91	*Spitzer*	ISAAC	16 34 29.3	−15 47 01.4	5650432
W33A	*ISO* SWS	*ISO* SWS	18 14 39.7	−17 52 02.0	32900920
GL 2136	*ISO* SWS	*ISO* SWS	18 22 27.0	−13 30 10.0	33000222
Serp S68	*Spitzer*	...	18 29 48.1	+01 16 42.5	9828608
EC 74	*Spitzer*	NIRSPEC	18 29 55.7	+01 14 31.6	9407232
EC 82	*Spitzer*	ISAAC	18 29 56.9	+01 14 46.5	9407232
SVS 4-5	*Spitzer*	ISAAC	18 29 57.6	+01 13 00.6	9407232
EC 90	*Spitzer*	ISAAC	18 29 57.8	+01 14 05.9	9828352
SVS 4-10	*Spitzer*	ISAAC	18 29 57.9	+01 12 51.6	9407232
CK 4	*Spitzer*	NIRSPEC	18 29 58.2	+01 15 21.7	9407232
CK 2	*Spitzer*	ISAAC	18 30 00.6	+01 15 20.1	11828224
RCrA IRS 5	*Spitzer*	ISAAC	19 01 48.0	−36 57 21.6	9835264
RCrA IRS 7A	*Spitzer*	ISAAC	19 01 55.3	−36 57 22.0	9835008
RCrA IRS 7B	*Spitzer*	ISAAC	19 01 56.4	−36 57 28.0	9835008
CrA IRAS 32	*Spitzer*	...	19 02 58.7	−37 07 34.5	9832192
S140 IRS 1	*ISO* SWS	NIRSPEC	22 19 18.4	+63 18 45.0	22002135
NGC 7538 IRS 9	*ISO* SWS	NIRSPEC	23 14 01.7	+61 27 20.0	09801532
IRAS 23238+7401	*Spitzer*	...	23 25 46.7	+74 17 37.2	9833728

NOTE.—Units of right ascension are hours, minutes, and seconds, and units of declination are degrees, arcminutes, and arcseconds.

TABLE 2
NEW CO ICE BAND OBSERVATIONS

Source	τ(CO : H_2O) (Red)[a,b]	τ(Pure CO) (Middle)[c]	τ(CO : CO_2) (Blue)[d]
W3 IRS 5	0.11 ± 0.05	0.27 ± 0.06	0.06 ± 0.05
L1448 IRS 1	0.10 ± 0.05	0.18 ± 0.06	0.09 ± 0.03
RNO 15	0.12 ± 0.03	0.27 ± 0.03	0.09 ± 0.03
IRAS 03254+3050	0.12 ± 0.06	0.19 ± 0.10	0.11 ± 0.05
IRAS 03271+3013	<0.5	1.0 ± 0.5	<0.5
B1-a	<0.5	4.0 ± 2.0	<0.3
IRAS 03439+3233	0.09 ± 0.05	0.25 ± 0.10	0.08 ± 0.04
IRAS 03445+3242	0.30 ± 0.05	1.16 ± 0.20	0.30 ± 0.03
DG Tau B	0.13 ± 0.05	0.12 ± 0.10	0.11 ± 0.05
GL 989	0.19 ± 0.03	0.37 ± 0.05	0.16 ± 0.05
HH 46 IR	0.80 ± 0.08	0.68 ± 0.06	0.16 ± 0.05
GY 224	<0.2	<0.2	<0.2
IRS 37	0.08 ± 0.02	0.45 ± 0.04	0.10 ± 0.05
GL 2136	0.20 ± 0.05	0.10 ± 0.05	<0.05
EC 74	<0.10	0.75 ± 0.06	0.10 ± 0.06
CK 4	<0.03	0.48 ± 0.05	0.07 ± 0.03
S140 IRS 1	0.05 ± 0.02	0.04 ± 0.02	<0.03
NGC 7538 IRS 9	0.52 ± 0.05	3.17 ± 0.10	0.30 ± 0.03

[a] Decomposition as described in Pontoppidan et al. (2003b).
[b] Adopted conversion to column density: $N_{CO:H_2O} = (16.0\ cm^{-1})\tau_{CO:H_2O}A^{-1}$, where $A = 1.1 \times 10^{-17}$ cm molecule^{-1} is the CO band strength.
[c] Adopted conversion to column density, using a continuous distribution of ellipsoids (CDE): $N_{CO} = (6.0\ cm^{-1})\tau_{CO}A^{-1}$.
[d] $N_{CO:CO_2} = (3.0\ cm^{-1})\tau_{CO:CO_2}A^{-1}$.

are derived using the 3.08 μm ground-based spectra or taken from Paper I. The data set is summarized in Table 1. The new observations of the CO ice bands not covered in Pontoppidan et al. (2003b) are summarized in Table 2.

4. PROFILE DECOMPOSITION

4.1. *Continuum Determination*

To directly compare with dust models, the spectra of ice absorption bands have to be converted to an optical depth scale. This requires that an appropriate continuum be defined, a process somewhat complicated for CO_2 by the location of the bending mode on the blue side of the broad silicate bending mode and on the red side of the H_2O libration band. Unfortunately, not knowing the shape of the underlying continuum, this is a problem with no unique solution. In this work, continua for each spectrum are constructed by fitting a third-order polynomial to the spectral ranges 13–14.7 and 18.2–19.5 μm. The shape of the blue wing of the silicate bending mode is simulated by a Gaussian in frequency space with center at 608 cm^{-1} and an FWHM of 73 cm^{-1}. The aim is to construct a shape of the continuum that has a negative second derivative under the CO_2 band. The same procedure has been used for all the *Spitzer* spectra, and the resulting continua are shown for each spectrum in Figure 4 below.

4.2. *Laboratory Data*

A number of laboratory spectra of CO_2 ices have been taken from the literature. Ice inventories of envelopes around young low-mass stars have shown that the ices are dominated by H_2O, CO, and CO_2, so this study concentrates on systems involving these three species. In some regions of low-mass star formation, CH_3OH is found in large amounts (up to 25% relative to H_2O), but this seems to affect only a small subset of the sample presented here.

The available laboratory spectra are divided into CO_2 : H_2O mixtures and CO_2 : CO mixtures, each set with distinct characteristics. As in the case of all solid-state features due to abundant molecules, the band shapes can be strongly modified by surface modes, depending on the shape distribution of the dust grains (Tielens et al. 1991). Astronomical spectra can therefore not be directly compared to absorbance laboratory spectra. Rather, complex refractive indices must be combined with a dust model to calculate opacities relevant for the small irregular dust grains of the interstellar medium. This study is consequently restricted to laboratory experiments for which optical constants have been calculated.

Ehrenfreund et al. (1997) and Dartois et al. (1999) present optical constants for a wide range of CO_2 : CO mixtures, as well as a few CO_2 : H_2O mixtures, obtained under high-vacuum (HV) conditions and 2.0 cm^{-1} resolution. More recently, a number of detailed studies of relevant CO_2-rich ices were performed by van Broekhuizen et al. (2006) and Öberg et al. (2007a) also under HV conditions. While these studies do not provide optical constants directly, they do report absorbance spectra, as well as approximate ice thicknesses, making it possible to derive optical constants using the Kramers-Kronig relations.

For the H_2O-rich ices, the CO_2 : H_2O = 14 : 100 mixture at 10 K from Ehrenfreund et al. (1997) was chosen. The CO-rich ices show a CO_2 bending model profile that is dependent on the mixing ratio. A function is therefore constructed that returns an ice spectrum for any relative concentration between CO_2 : CO = 1 : 4 and CO_2 : CO = 1 : 1 by interpolating between the available 10 K laboratory spectra within this range. At very low concentrations of CO_2 relative to CO (CO_2 : CO < 1 : 10), the bending mode becomes quite narrow, and the shape becomes independent of concentration. At very high concentrations of CO_2, the bending mode exhibits the well-known split, characteristic of a crystalline structure of the ice. The peaks are very narrow (of order 1 cm^{-1}), and so the higher resolution data from van Broekhuizen et al. (2006) are used for pure CO_2 ice. This spectrum, however, suffers from a misalignment in the spectrometer optics at 0.5 cm^{-1} resolution so that the bending mode is too weak by a factor of 3 relative to the stretching mode and the noise is relatively high. As a result, it was necessary to scale

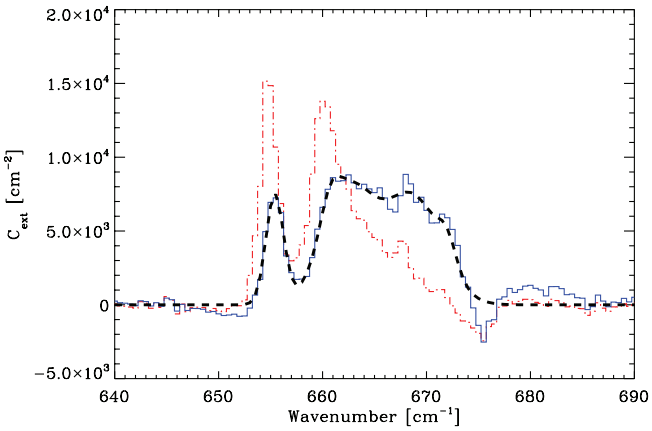

FIG. 1.—Comparison of the absorbance spectrum of van Broekhuizen et al. (2006) relevant for pure CO_2 ice (*red dot-dashed line*) with that calculated for a CDE distribution of particles in the Rayleigh limit (*blue solid line*). The dashed line shows the component fit used to eliminate the noise.

the absorbance of the bending mode to fit with the band strength of 1.1×10^{-17} cm^{-1} reported by Gerakines et al. (1995) before calculating the corresponding set of optical constants. The noise in the spectrum is reduced by fitting a number of Gaussians, rather than smoothing it, which would reduce the resolution. Because all the laboratory spectra used were obtained under high-vacuum conditions, they may be contaminated by H_2O.

At 15 μm the dust grains are most likely well into the Rayleigh limit of $2\pi a \ll 15$ μm, where a is the radius of the largest grains. This means that scattering of light out of the line of sight is unimportant, and the opacities can be treated as pure absorption coefficients. A continuous distribution of ellipsoids (CDE) is used to convert the optical constants to opacities. This is a convenient method of simulating the effect of irregularly shaped grains, found to work well for ice bands in the Rayleigh limit, and it has been used successfully for solid CO (Pontoppidan et al. 2003b) and CO_2 (Gerakines et al. 1999). Figure 1 illustrates the process of converting the absorbance spectrum of pure CO_2 into an opacity that can be used for comparing with the *Spitzer* spectra. The laboratory spectra are summarized in Table 3.

4.3. *Component Analysis*

The strategy adopted here for analyzing the general shape of the CO_2 ice bending mode in low-mass young stellar envelopes is to determine the minimum number of unique components required to fit all of the observed bands. In this context, a unique component is a band that only changes its relative depth, but not its shape from source to source. This approach was used in

TABLE 3
LABORATORY SPECTRA

Mixture	T (K)	Resolution (cm^{-1})	References
CO_2 : H_2O = 14 : 100	10	2	1
CO_2 : CO = 4 : 100	10	2	1
CO_2 : CO = 26 : 100	10	2	1
CO_2 : CO = 70 : 100	10	2	1
CO_2 : CO = 112 : 100	10	2	1
Pure CO_2	15	0.5	2

REFERENCES.—(1) Ehrenfreund et al. 1997; (2) van Broekhuizen et al. 2006.

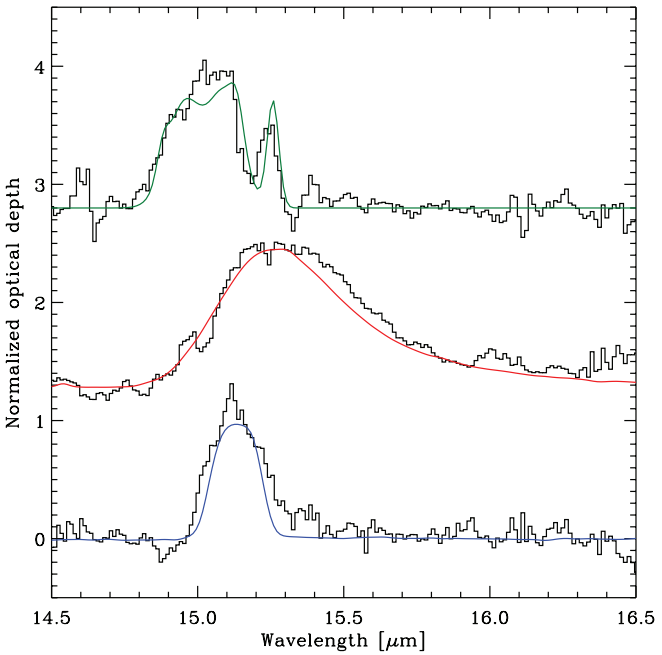

FIG. 2.—Empirically determined profiles for the three dominant components of the CO_2 bending mode. The data are as follows. *Top*: RNO 91–IRS 42, fitted using pure CO_2. *Middle*: CRBR 2422.8−3423–IRS 51, fitted using CO_2 : H_2O = 14 : 100. *Bottom*: IRS 63–IRS 42, fitted using CO_2 : CO = 26 : 100.

Pontoppidan et al. (2003b) to determine that only three unique components could be used to fit the 4.67 μm stretching mode of solid CO, and it is also used in Paper I to decompose the 5–8 μm complex. The three unique CO components were (1) a broad, redshifted component associated with CO in a water-rich mantle, (2) a component indistinguishable from pure CO, and (3) a narrow, blueshifted component due to either CO in a CO_2 environment or CO in a crystalline form. The three CO components were named "red," "middle," and "blue," and as seen below, the red and blue components have counterparts in the CO_2 bending modes. Note that the red and middle components are also often referred to in the literature as "polar" and "nonpolar," respectively. The bending mode of CO_2 probes ice structures that are somewhat more complicated than those probed by CO. While most of the CO ice desorbs efficiently at temperatures higher than 20 K, the less volatile CO_2 ice goes through several additional structural changes. The most characteristic is the appearance of the double peak seen in pure CO_2 (see Fig. 1).

In order to empirically derive the shape of the components of the CO_2 bending mode, pairs of spectra are subtracted. If the spectra are superpositions of a small number of components with varying relative contributions, it will be possible to isolate each component. The three dominant components determined this way are shown in Figure 2, where they are compared to laboratory simulations.

Consequently, it is found that the minimum number of unique components required to fit all the observed CO_2 bending mode profiles is five:

1. An H_2O rich component, modeled with a laboratory spectrum with a concentration of CO_2 : H_2O = 14 : 100. This is required to fit the red wing of almost all of the observed bands. This is referred to as the red component.
2. A component with a roughly equal mixture of CO_2 and CO. Strictly speaking, this is not constructed as a unique component since the CO_2 : CO mixing ratio is included as a free

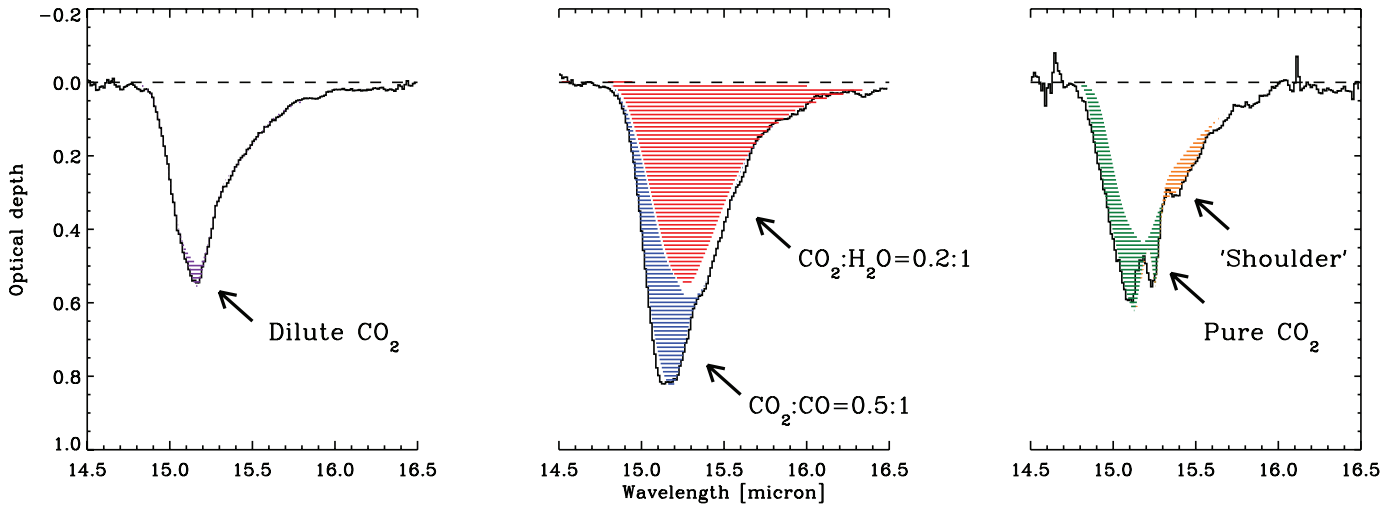

FIG. 3.—Sketch of the five different components used to fit the CO_2 band. The spectra used to illustrate the components are (*left to right*) IRS 51, SVS 4-5, and RNO 91.

parameter. This is required because the empirical profiles of the blue component, one of which is shown in Figure 2, have varying widths. This behavior can be reproduced by varying the concentration of CO_2 in CO. While the band profiles are only available for a set of discrete mixing ratios, profiles are constructed with arbitrary mixing ratios by linearly interpolating the available laboratory profiles at each frequency point. In effect, this allows a measurement of the CO_2:CO mixing ratio for each observed CO_2 bending mode. This is referred to as the blue component.

3. A component in which CO_2 is very dilute in an otherwise pure CO ice. This is a very narrow component centered on 15.15 μm (660 cm^{-1}). In practice, this band is modeled by a $CO_2:CO = 4:100$ laboratory spectrum. Note that at such high dilution, the shape of the band is not sensitive to the exact mixing ratio.

4. A component of pure CO_2, producing the characteristic double-peaked structure often seen in protostellar sources.

5. An additional, relatively narrow component on the red side of the main band. This component is unambiguously identified in only a few sources, most of them the massive young stars included from the *ISO* sample. The component has in the past been identified as an interaction with CH_3OH in strongly annealed ices with the mixing ratio $H_2O:CO_2:CH_3OH = 1:1:1$ (Gerakines et al. 1999). Since there is no laboratory spectrum of the shoulder in isolation, the component is modeled empirically using a superposition of two Gaussians:

$$\tau_{\rm shoulder}(\nu)/\tau_0 = \exp\left[\frac{-(\nu - 645\ {\rm cm}^{-1})^2}{2(2.1\ {\rm cm}^{-1})^2}\right] + 1.85\exp\left[\frac{-(\nu - 650\ {\rm cm}^{-1})^2}{2(2.8\ {\rm cm}^{-1})^2}\right],$$

where τ_0 is a scale factor.

The red and blue components generally dominate the bending mode profiles and the total CO_2 abundance. The remaining three components represent subtle differences due to trace constituents. It is stressed that all the components correspond to distinct and plausible molecular environments. The relative contributions to three typical CO_2 bending mode profiles are sketched in Figure 3.

A nonlinear least-squares fitting routine from the IDL library of C. Markwardt[8] is used to find the best fit to each bending mode spectrum. Since three of the five components used to interpret the CO_2 spectrum include CO, each fit in part predicts a corresponding CO stretching mode spectrum. This information is used to construct a model CO ice spectrum that can be compared directly with the observed 4.67 μm CO bands. The model CO profiles are therefore only fitted to the CO_2 bending mode profiles and are plotted on the observed CO profiles for comparison only. In summary, each 15.2 μm CO_2 bending mode is fitted with a function with six free parameters: the depth of the five components and the mixing ratio of CO_2 to CO for the blue component. The spectra and best fits are shown in Figures 4 and 5, along with the CO stretching mode bands, where available. The CO_2 column densities are given in Table 4.

It is found that the blue CO stretching mode band corresponding to the blue CO_2:CO mixture was in general much too deep to fit the observed CO bands, and it has consequently been reduced by a factor of 3 relative to the CO_2 bending mode in the comparison plots for all of the sources. This discrepancy is discussed in § 5.3. In this paper the same band strength of 1.1×10^{-17} cm molecule^{-1} is used for every component of CO_2. Note that while Gerakines et al. (1995) measure a larger band strength for the CO_2 bending mode in a water-rich environment of 1.5×10^{-17} cm molecule^{-1}, they also state that a large uncertainty is associated with this measurement. The effect of using this band strength for CO_2 in a water-rich mixture would be to decrease the CO_2 column density of the red component by 36%.

5. RELATIONS OF THE CO_2 COMPONENTS

5.1. *The Abundance of* CO_2 *Ice in Low-Mass YSO Envelopes*

The relation between the observed H_2O ice column densities and the total CO_2 ice column densities is shown in Figure 6. Because it is difficult to measure the column density of H_2 gas along the line of sight, this is the relation typically used to define the *ice abundance* of a given solid-state species as a number fraction

[8] See http://cow.physics.wisc.edu/~craigm/idl/idl.html.

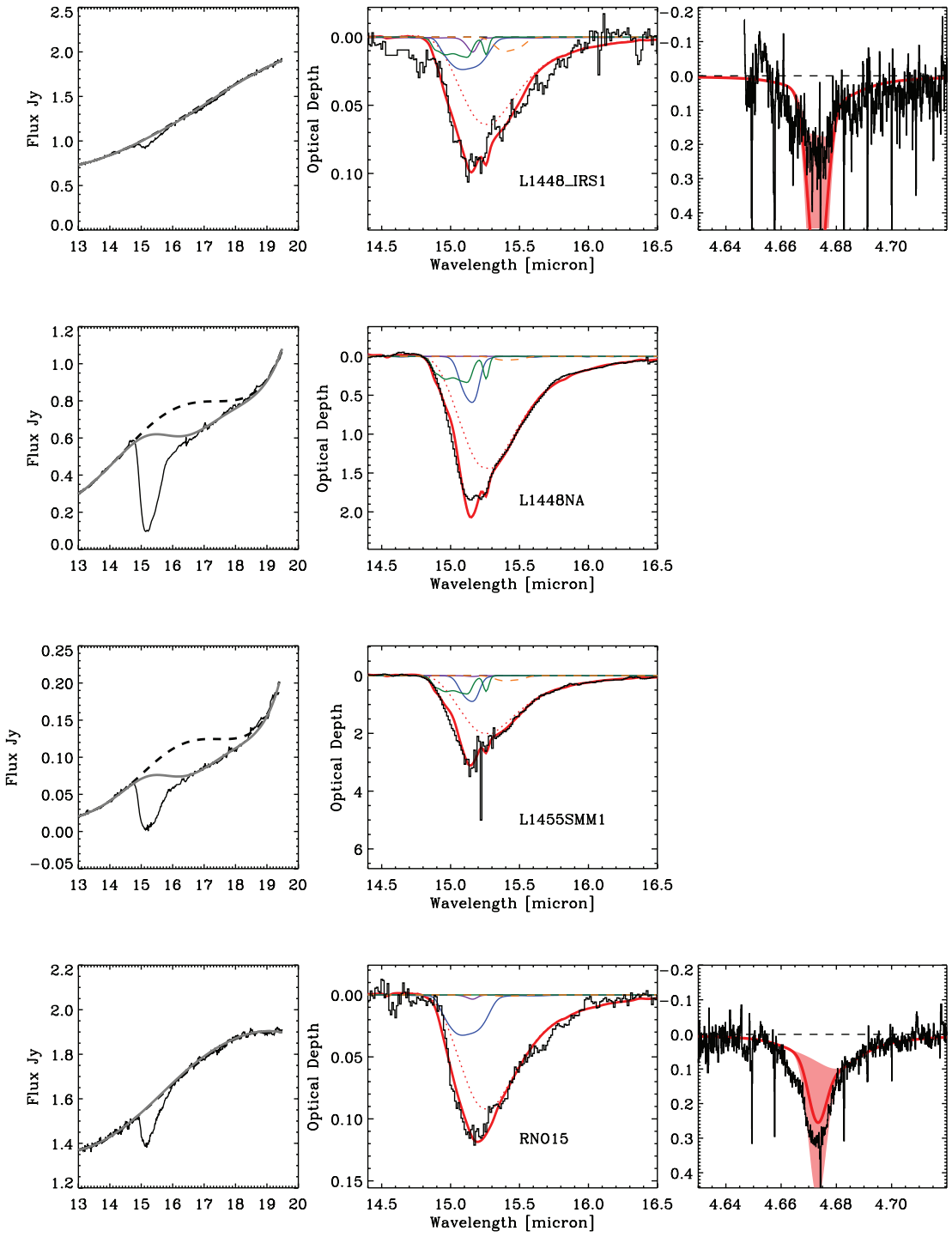

FIG. 4.—*Left*: Continuum determinations for the SH spectra. The dashed lines are low-order polynomial fits, while the solid lines are the fits with a Gaussian included to simulate the blue wing of the 18 μm silicate bending mode. *Middle*: Component fits of the CO_2 bending mode profiles. *Right*: CO stretching mode profiles predicted by the fit to the CO_2 bending mode (where available). The components are discussed in § 4.3. The shaded areas indicate the profiles allowed by the uncertainties in the fit to the CO_2 bending modes.

relative to water ice. The CO_2 ice abundance is remarkably constant but does exhibit a scatter that is much larger than the uncertainties. A linear fit to the low-mass stars reveals a number ratio of CO_2 to H_2O to be 0.32 ± 0.02, with a Pearson correlation coefficient of 96%. There is, however, a significant scatter in the relation, and a number of our sources show abundances between 0.2 and 0.3, relative to H_2O. The relation exhibits a slight tendency for higher CO_2 abundances at higher H_2O column densities.

The CO_2 abundance derived here can be compared with that of 0.17 for the *ISO* sample of massive YSOs (Gerakines et al. 1999) and 0.18 ± 0.04 for quiescent clouds as observed toward background stars (Whittet et al. 2007). Both these samples have been included in Figure 6. The points associated with the massive YSOs thus indicate a significantly lower CO_2 abundance. Inspection of the figure also reveals that the background stars generally probe lower column densities than the YSOs. For these

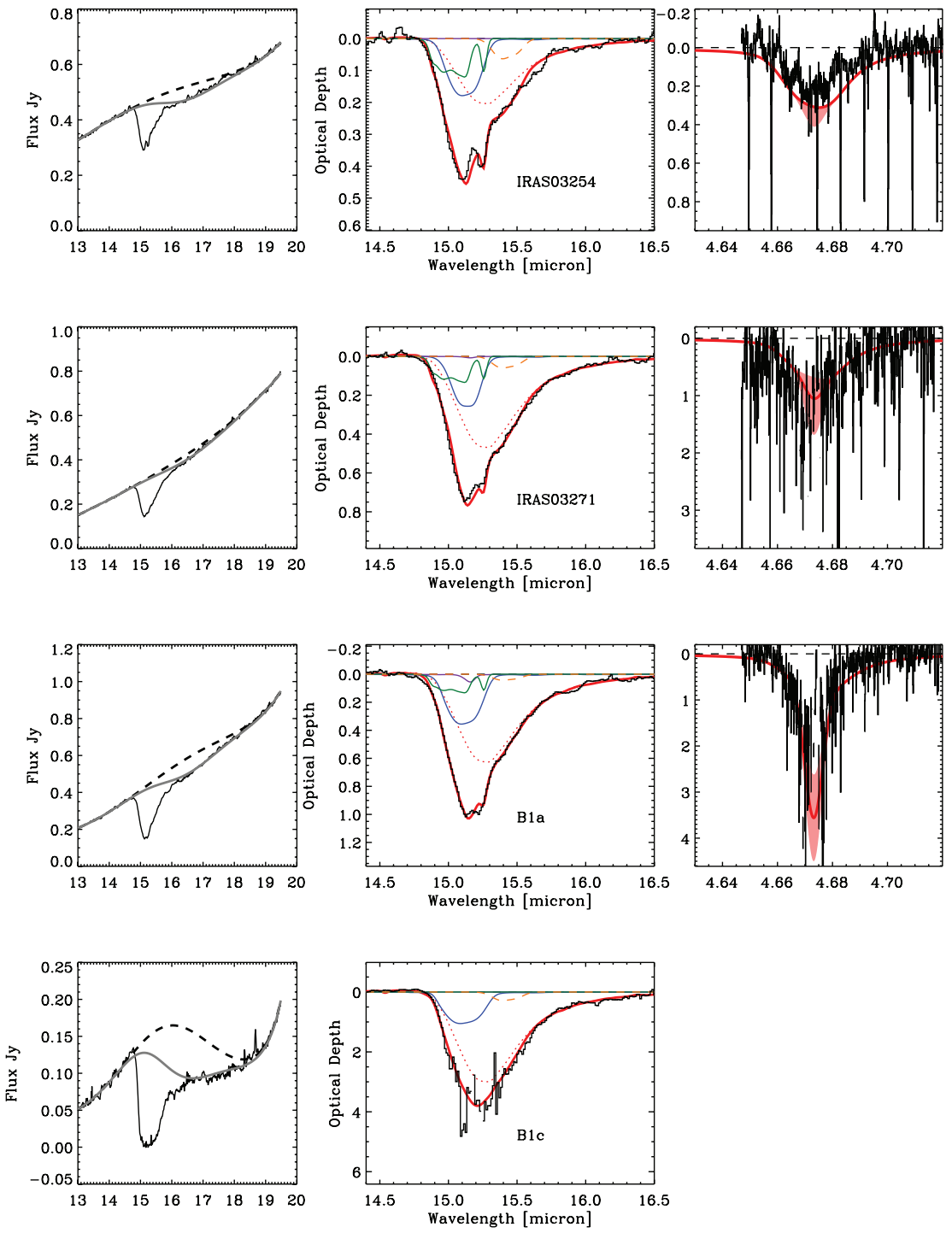

FIG. 4—*Continued*

low column densities, the difference between the YSOs and the background stars is less significant. However, at water ice column densities higher than $\sim 2 \times 10^{18}$ cm^{-2}, the difference in CO_2 abundance between background stars at low A_V and low-mass YSOs is highly significant. This sudden change in the relation may represent the activation of a new formation route to CO_2 in addition to that forming the $H_2O : CO_2$ mantle at lower A_V. An increase of CO_2 abundance in denser regions of a single cloud core was observed by Pontoppidan (2006) and was also discussed for the background stars in Whittet et al. (2007) based on a single star at high A_V.

5.2. *The* $CO_2 : H_2O$ *System*

The $CO_2 : H_2O$ component dominates every CO_2 bending mode band, and the abundance variation of this component, or lack thereof, therefore mimics that of the total CO_2 band discussed in § 5.1. In the following, "abundance" refers to an observed column density ratio averaged over the line of sight, while "concentration" is the local point number density of a species relative to the total number density of molecules in an ice film. The abundance of this component varies between 0.1 and 0.3 relative to water, with a median value around 0.2. If the concentration

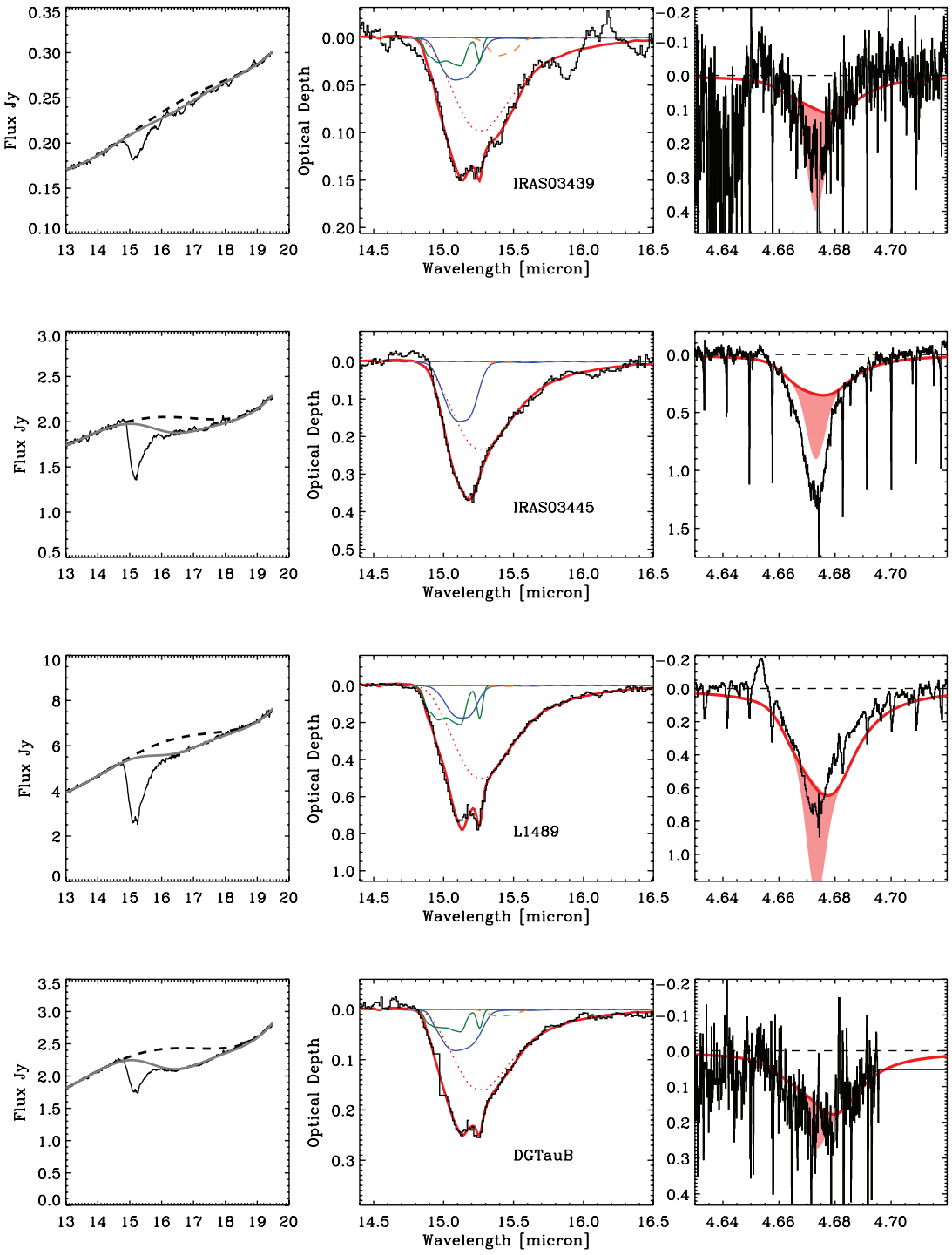

FIG. 4—*Continued*

equals the abundance, the relevant mixing ratio for a laboratory analog is $CO_2:H_2O = 1:5^{+5}_{-2}$. The observed abundances of the $CO_2:H_2O$ component are shown in Figure 7 as a function of the corresponding $CO:H_2O$ component of the CO stretching mode.

The general value of this parameter is of some importance. Öberg et al. (2007a) showed that the band strengths of the various H_2O modes are very sensitive to the CO_2 concentration, and they suggested that this may be an explanation for the discrepancy in observed band depths between the H_2O stretching and bending modes. The observed abundances of the $CO_2:H_2O$ component suggest that the influence of CO_2 may explain a part of the H_2O bending/stretching mode discrepancy. This is discussed in greater detail in Paper I.

5.3. *The* CO_2:CO *System*

5.3.1. *The "Blue" Component*

The component fit indicates that the $CO_2:CO$ system forms a component separate from the CO_2 mixed with water. The evidence is the higher abundance of the CO-dominated component in dense, cold cloud regions as discussed in Pontoppidan (2006)

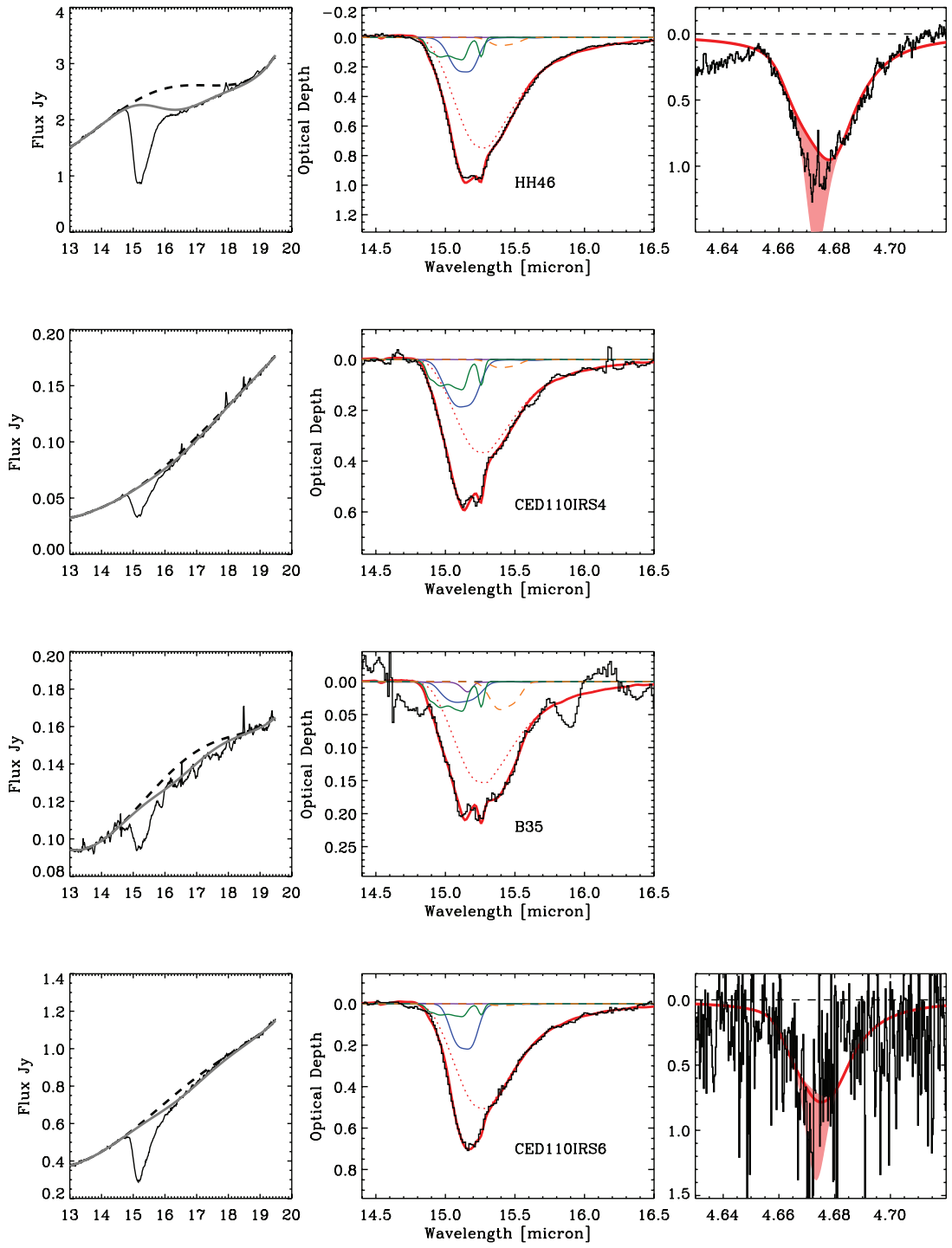

FIG. 4—*Continued*

and as suggested by the offset of low-mass protostellar envelopes relative to background stars and massive YSOs in Figure 6, as well as the match of the profile of this blue CO_2 component with laboratory simulations of CO_2:CO mixtures. An important parameter to determine is the concentration of CO_2 relative to CO in this component. There are at least two ways of doing this. First, the concentration can be directly determined by comparing the observed strength of the blue CO_2 component with the corresponding blue component of CO observed as part of the CO stretching mode band. Second, it can be indirectly inferred by the profile of the CO_2:CO component of the CO_2 bending mode, since this is sensitive to the concentration.

The column density ratios of the CO_2 and CO blue components are illustrated in Figure 8. These components exhibit a fairly strong correlation with a Pearson correlation coefficient of 0.70 and a slope of $N(\text{blue } CO_2)/N(\text{blue CO}) = 2.5 \pm 0.2$, assuming a width of 3 cm^{-1} for the blue CO component as empirically determined in Pontoppidan et al. (2003b). The laboratory spectra of the CO stretching mode of CO_2:CO mixtures are about twice as wide. Using the laboratory spectra instead to

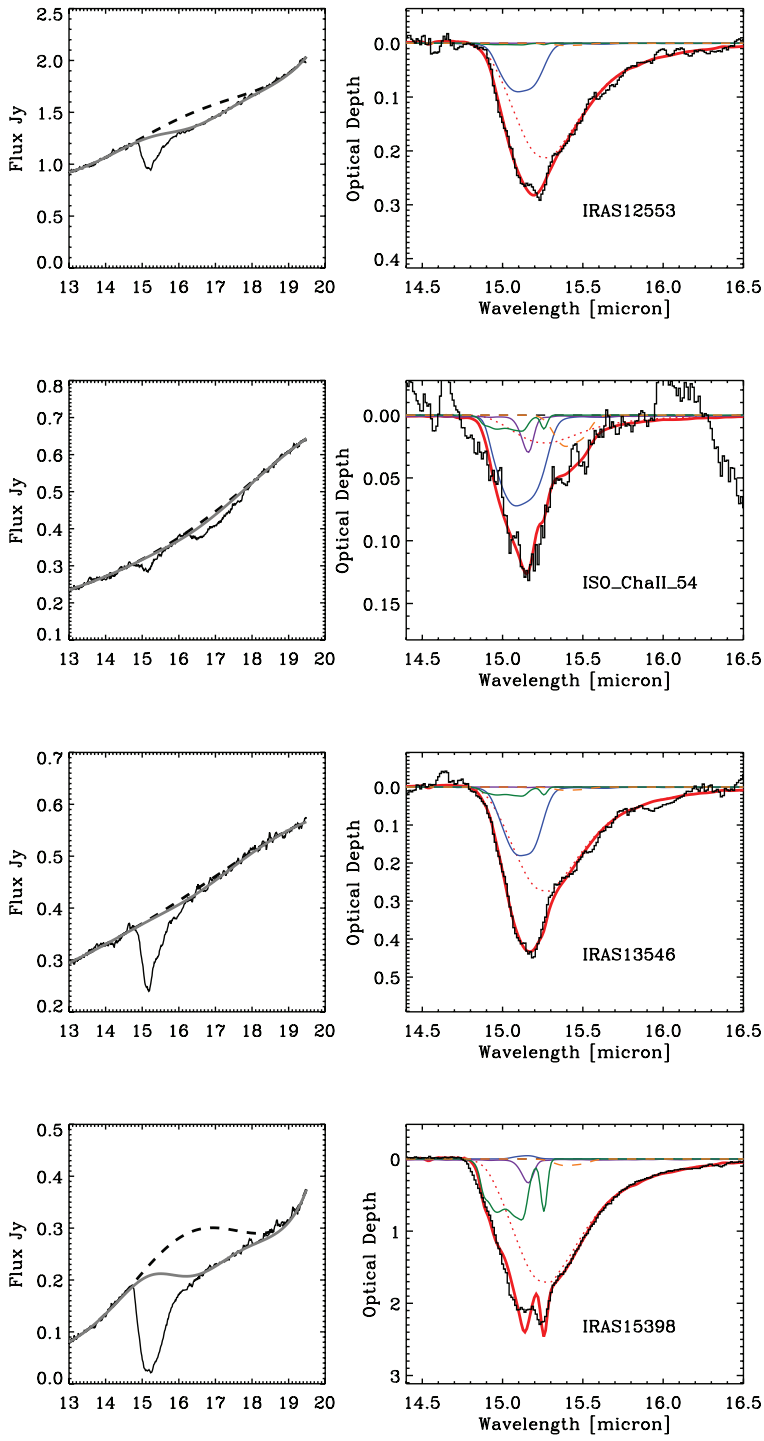

FIG. 4—*Continued*

calculate the column densities of the blue CO component would decrease this ratio to 1.25 ± 0.1.

Conversely, Figure 9 illustrates the indirect method of determining the concentration of CO_2 in CO from the profile of the blue CO_2 component. The figure shows the distribution of CO_2:CO mixing ratios as determined by the component fit. It is seen that the mixing ratios are remarkably similar for most of the observed spectra, which is also indicated by the direct correlation seen in Figure 8. However, the median concentration determined using this method is $N(\text{blue } CO_2)/N(\text{blue CO}) = 0.55 \pm 0.2$, or a factor of 2–5 smaller than that determined using the directly measured column densities.

It is probably reasonable to assume that the direct method provides a better estimate of the concentration since the indirect method relies on an uncertain calibration of a set of laboratory experiments. However, it should be noted that the band strengths of both CO_2 and CO may depend on concentration, which is an effect that is ignored here by assuming that the band strengths are constant. Variable band strengths may affect the direct method. Clearly, well-calibrated laboratory experiments are needed to

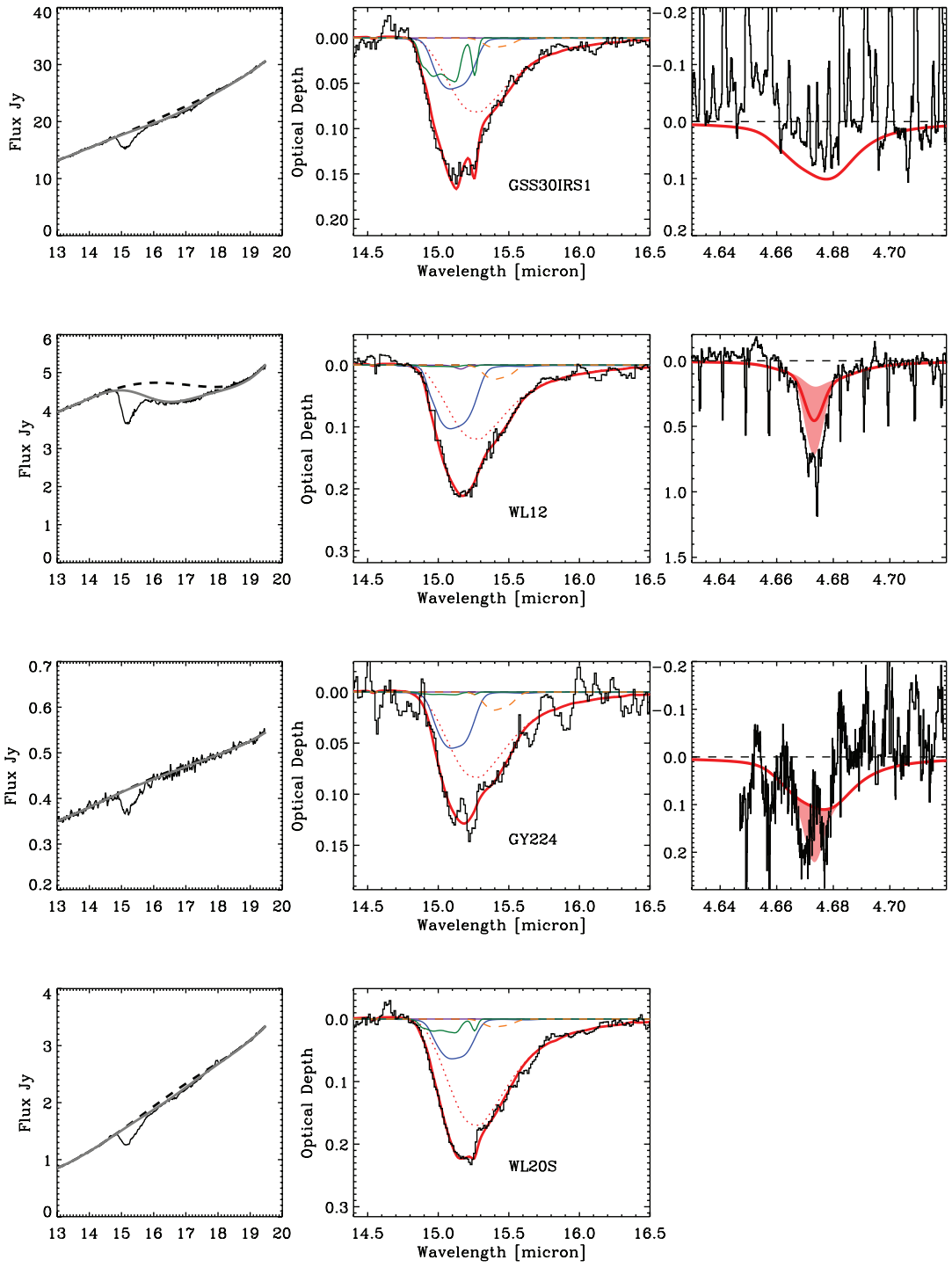

FIG. 4—*Continued*

resolve the issue. For this study, the blue CO components, as determined by the profile of the blue CO_2 band, are divided by a factor of 3 to better match the CO bands, as dictated by the direct concentration measurement. Note that Pontoppidan et al. (2003b), in their study of the CO stretching vibration band at 4.67 μm, found that the available laboratory spectra of CO_2:CO mixtures were generally much too wide to reproduce the blue wing of the CO bands, as confirmed by van Broekhuizen et al. (2006), which led them to consider alternatives to explain the blue component of the CO band. Here it is concluded, based on the clear correlation between the blue CO_2 and CO components, that they indeed represent the same component, but that since their detailed profiles do not fit well to the laboratory analogs, the structure of this component is not yet fully understood.

5.3.2. *The "Dilute" Component*

Some CO_2 bending mode profiles exhibit a very narrow single peak at 15.15 μm (660 cm^{-1}), as indicated in Figure 3. The most obvious sources with this property are IRS 51 and CRBR 2422.8−3423, as well as the background star CK 2. The

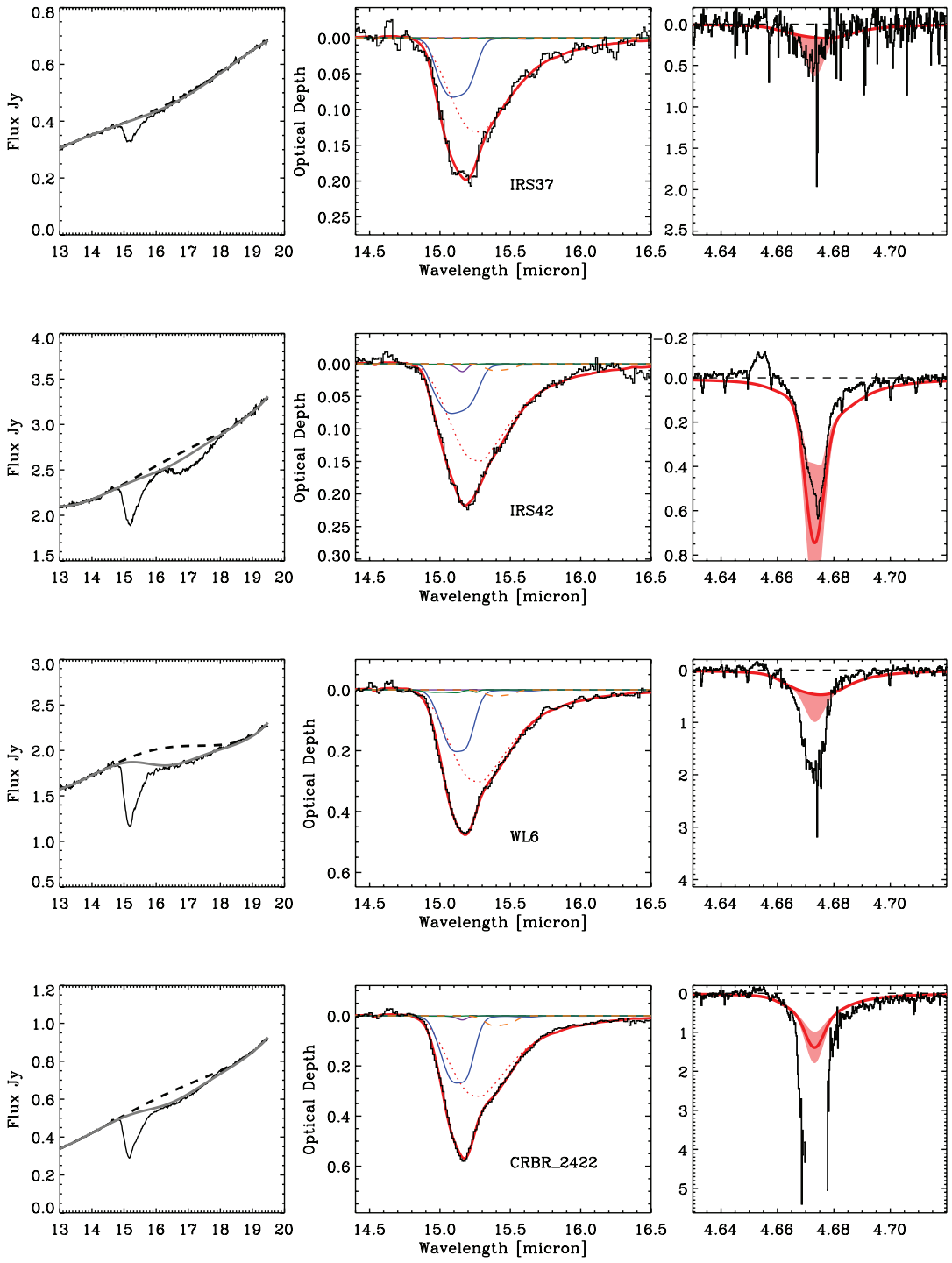

FIG. 4—*Continued*

profile of this component corresponds closely to that of a CO_2 ice very dilute in CO with a concentration less than 10%; the profile of the band does not change appreciably at lower concentrations. The "dilute" component typically appears toward sources that also have very large column densities of "pure" CO (the middle component of Pontoppidan et al. 2003b). The relation between these two components is shown in Figure 10, where it is seen that typical concentrations of CO_2 in the CO are 1:100–250. This indicates that there are vastly different mixing ratios of CO_2 to CO along each line of sight, possibly even on each grain.

5.4. *Relation with* CH_3OH

Because CH_3OH has been related to the shoulder on the red side of the CO_2 bending mode (Dartois et al. 1999), it is natural to estimate whether there is a connection with the direct measurement of CH_3OH abundances from Paper I. The relation, shown in Figure 11, does not exhibit an obvious relationship between the CO_2 shoulder and the CH_3OH abundance. This does not necessarily indicate that the shoulder is not related to interactions with CH_3OH if the concentration of CO_2 in the CH_3OH varies significantly. Keeping the assumption that the band strength

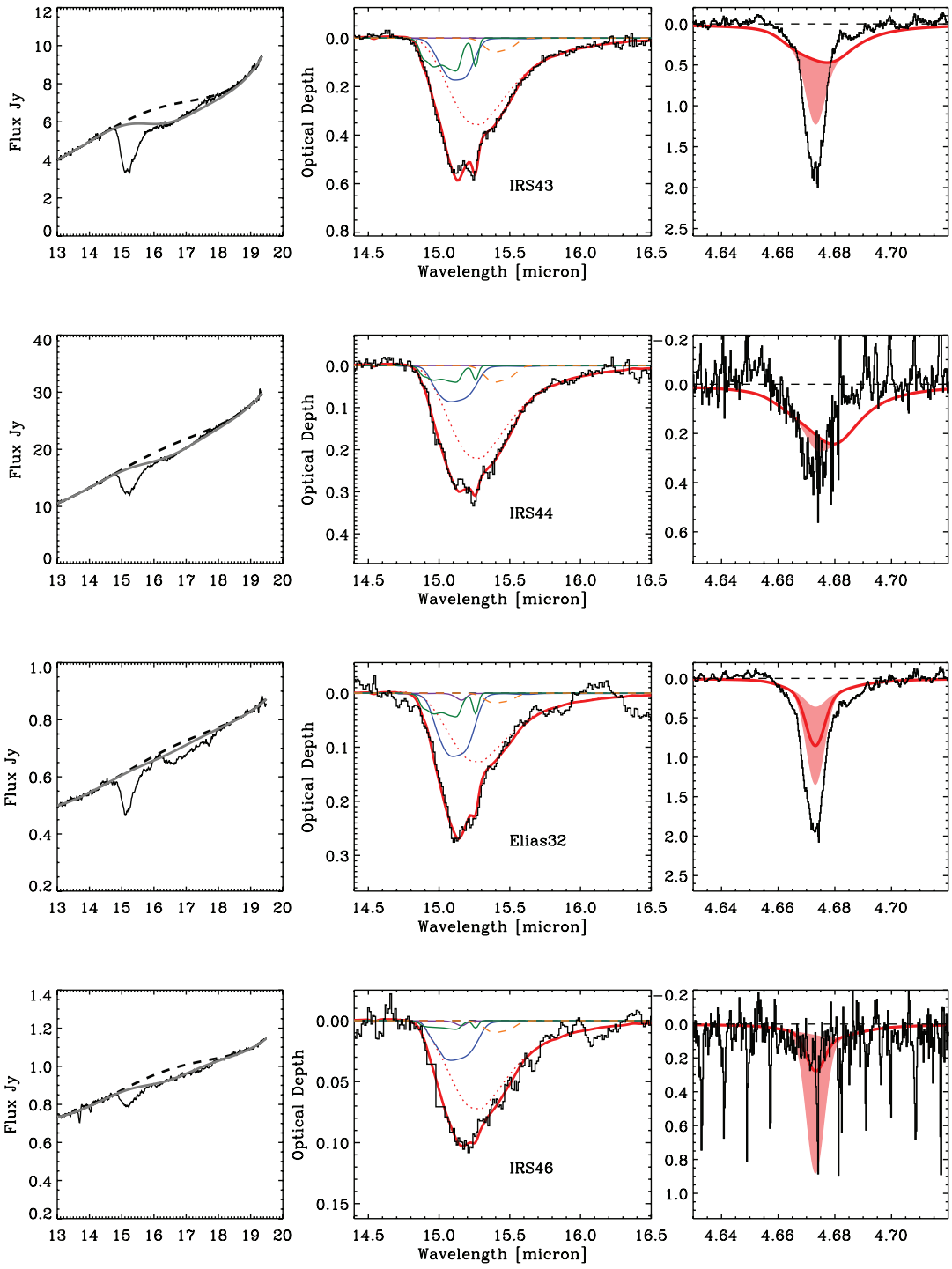

FIG. 4—*Continued*

of the CO_2 shoulder is that of pure CO_2, the abundance CO_2:CH_3OH varies between 1:20 and 1:3. It is therefore likely that the CO_2 is highly dilute in the CH_3OH ice.

5.5. *Upper Limits on* C_3O_2

Jamieson et al. (2006) found that carbon suboxide (C_3O_2) is formed in abundance along with CO_2 during electron irradiation of a CO ice. It has prominent bands around 17–19 μm (Gerakines & Moore 2001), but with exact central positions that vary considerably in the literature, presumably as a result of different ice mixtures. Some of the IRS spectra do have weak structure in the general wavelength region, but nothing that resembles a consistently recurring absorption band at a single wavelength. It is therefore concluded that there is no obvious evidence for absorption from C_3O_2 at the 5% level.

5.6. *The* 17 μm *Feature*

Some spectra show a clear excess absorption feature centered on 17 μm, most notably toward IRS 42, EC 90, VSSG 17, and ISO ChaII 54. The origin of this feature is unclear, and only its observed properties are reported here. It appears that there is some relation between the presence of the feature and sources that show contamination by silicate emission from the central disk. Thus, the feature may not be a real absorption signature, but

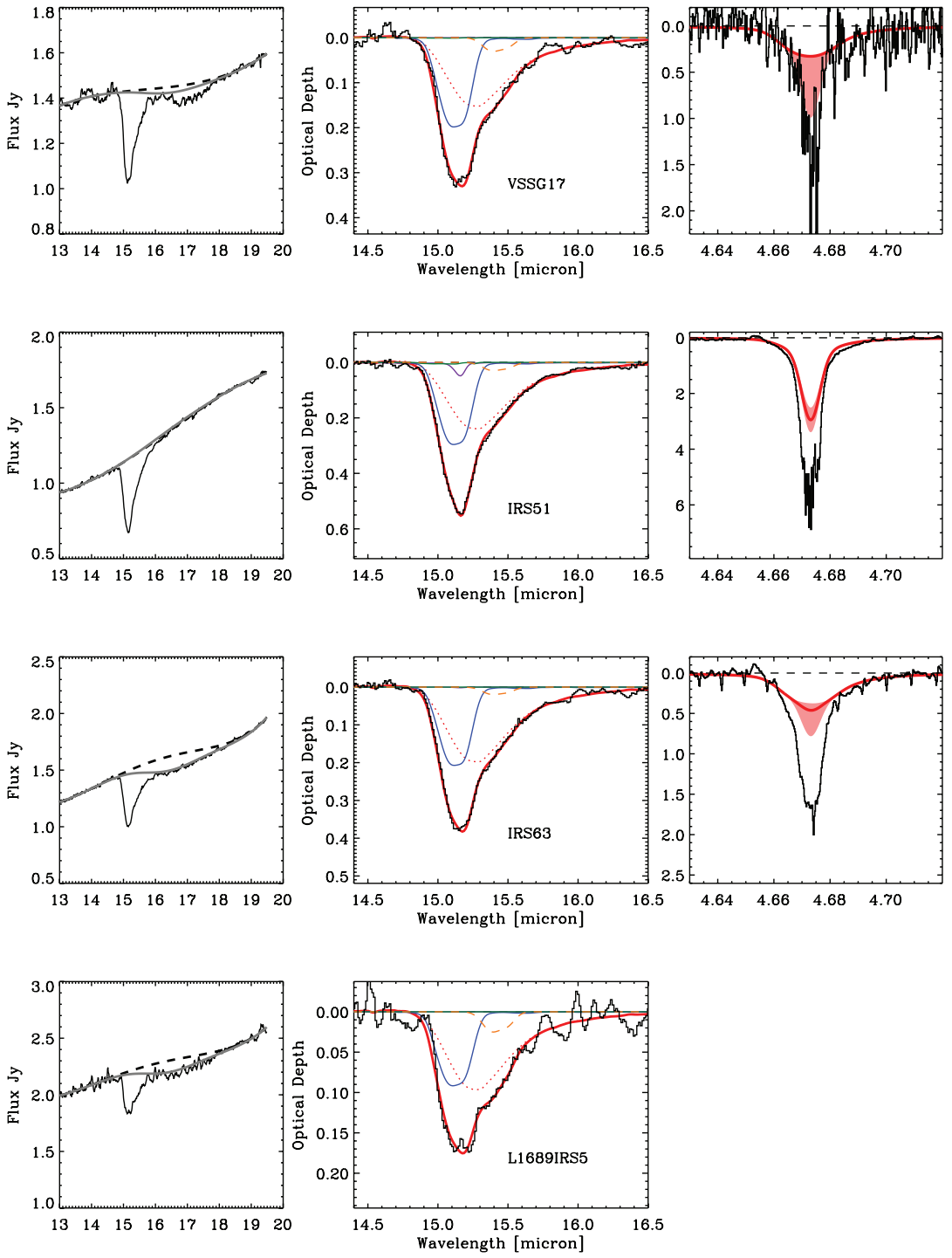

FIG. 4—*Continued*

emission from the 18 μm silicate band affecting the continuum determination. However, if real, the feature has a typical width of 35 cm^{-1} and optical depths of 0.1, where detected.

6. ORIGIN AND EVOLUTION OF THE CO_2 COMPONENTS

6.1. *Formation Routes to* CO_2 *in the Interstellar Medium*

CO_2 ice in protostellar envelopes as observed here is widely believed to be formed by surface reactions as opposed to a gas-phase route followed by freezeout (Tielens & Hagen 1982). Pure gas-phase chemical models of typical cold, dark clouds predict CO_2 abundances of 10^{-9} relative to H_2 (Bergin et al. 1995), making it unlikely that there is any contribution directly from gas-phase chemistry to the observed solid-state CO_2. There is strong observational evidence that CO_2 forms readily in cold quiescent molecular clouds, and it does not appear that "extra" photoprocessing of the ice is required, beyond what can be explained by cosmic-ray–induced UV photons and photons from the interstellar radiation field managing to penetrate to A_V values of 3–5 mag (Whittet et al. 1998). In fact, the relatively constant fraction of CO_2 relative to water ice (15%–40%) under a wide range of conditions suggests that it forms under "common" quiescent

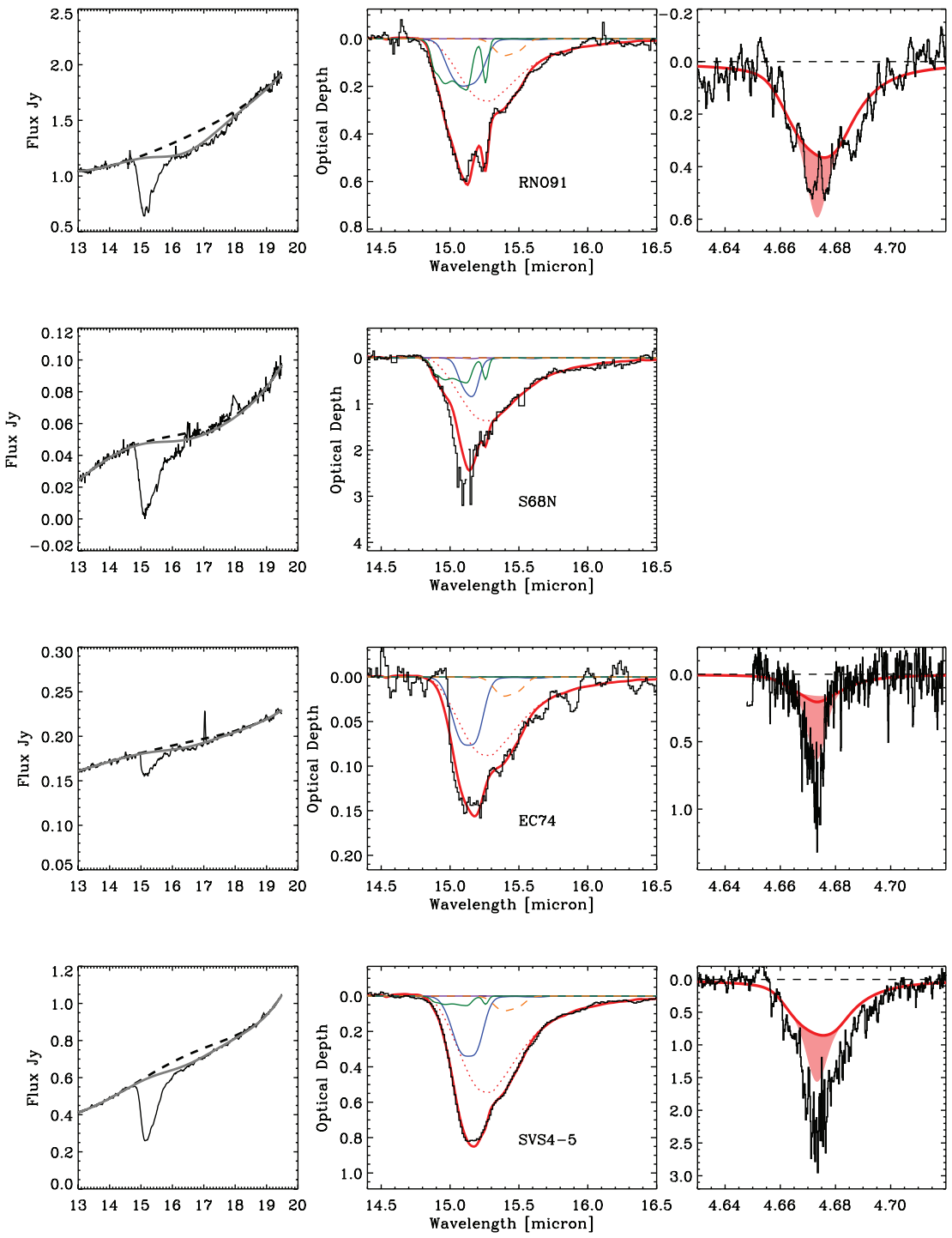

FIG. 4—*Continued*

conditions of densities of 10^4–10^5 cm^{-3}, temperatures near 10 K, and a standard cosmic-ray field. Thus far, no line of sight has been observed to have CO_2 abundances of $N_{CO_2}/N_{H_2O} \lesssim 0.15$. However, the exact chemical pathway remains controversial. Possible routes to the formation of CO_2 are via the reactions

$$CO + OH \rightarrow CO_2 + H, \quad (1)$$

$$O + HCO \rightarrow CO_2 + H, \quad (2)$$

$$CO + O \rightarrow CO_2. \quad (3)$$

Equation (3) is often included as an important grain surface reaction (Tielens & Hagen 1982; Stantcheva & Herbst 2004) but has also been found in at least one study to possess a prohibitively large barrier (Grim & d'Hendecourt 1986). However, a similar experiment by Roser et al. (2001) finds that the reaction proceeds with no or little barrier. It should be noted that it is expected that the barrier to equation (3) is sensitive to the electronic state of the oxygen atoms, such that $O(^1S)$ may react much easier with CO than oxygen in the ground state $O(^3P)$ (Fournier et al. 1979). The energy difference between these two states corresponds to a red photon (6300 Å), which will penetrate much

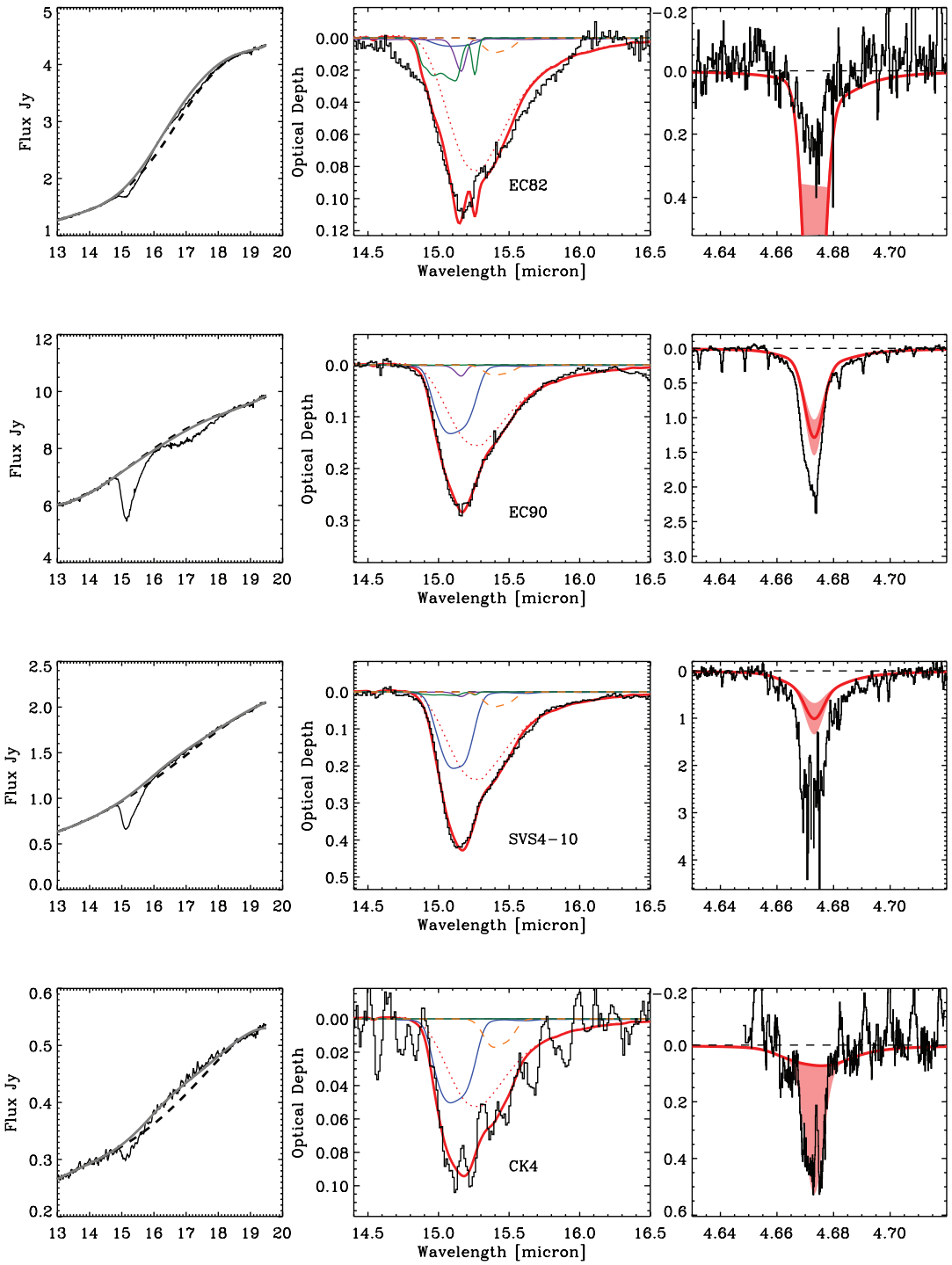

FIG. 4—*Continued*

deeper into dark clouds than the UV photons normally considered for photolysis reactions.

In some grain surface models, equation (1) is used as a dominant reaction (Chang et al. 2007).

It is also known that CO_2 can form with a low or nonexisting activation barrier through an electronically excited state of CO:

$$CO^* + CO \rightarrow CO_2 + C. \quad (4)$$

Obviously, this reaction requires that the CO molecule is excited, and it was studied extensively in the context of UV photolysis (e.g., Gerakines et al. 1996; Loeffler et al. 2005). However, Öberg et al. (2007b) find *no* formation of CO_2 from CO in an ultra–high-vacuum (UHV) UV irradiation experiment, which is much less contaminated by H_2O than the previous HV experiments. While this argues against equation (4) as an effective pathway to CO_2 ice, electron irradiation does produce CO_2 from pure CO under UHV conditions (Jamieson et al. 2006).

Consequently, the rates of most solid-state reactions leading to CO_2 are still controversial, and theoretical models have struggled to consistently reproduce the observed abundances. Based on existing observations, any model for the formation of CO_2

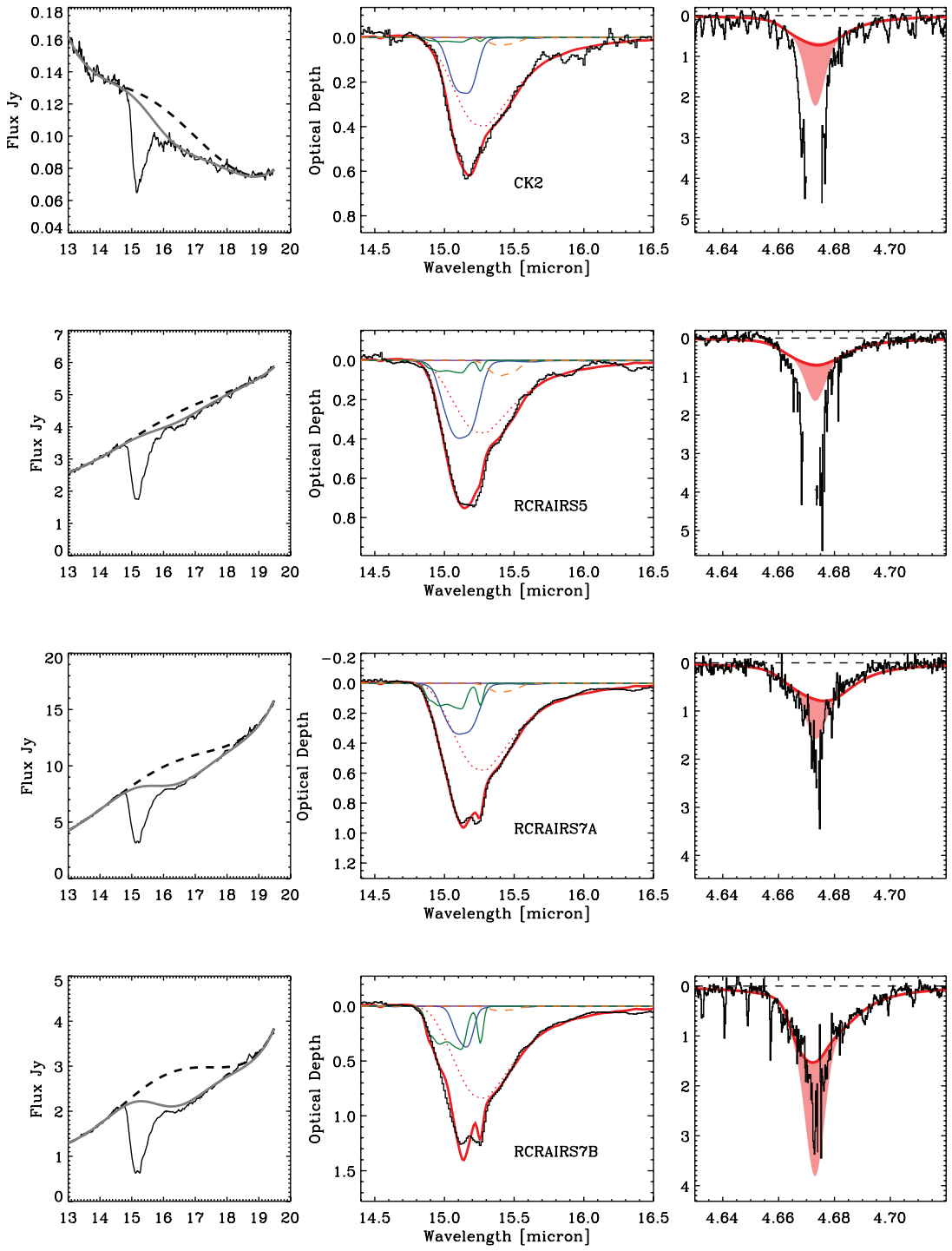

FIG. 4—*Continued*

should be required to reproduce both the absolute abundance of CO_2 of 15%–40% relative to water ice and the apparent universality of this abundance. In addition, the separate molecular environments of the CO_2 ice should also be explained, in particular the presence of CO_2 in both H_2O-rich and CO-rich environments.

It is worth mentioning that CO accreted from the gas phase is not the only potential source for the carbon in CO_2. Mennella et al. (2004) found that the carbon in hydrogenated carbon grains will form both CO and CO_2 when covered with a water ice mantle and subjected to cosmic rays. This is potentially a route to forming CO_2 embedded in a water ice matrix. However, having a different source of carbon for CO_2 formation than gas-phase CO must explain why the $^{12}C/^{13}C$ ratios of gas-phase CO, solid-state CO, and solid-state CO_2 are all so similar to the solar value of 89 (50–100; Boogert et al. 2000, 2002; Pontoppidan et al. 2003b). In contrast, presolar carbonaceous grains have highly variable $^{12}C/^{13}C$ ratios with a tendency toward ratios a few to 100 times that of the Sun, although some have ratios as low as $\sim$1 (e.g., Lin et al. 2002; Croat et al. 2005). The question is whether such scatter is reflected in the ice isotopologue ratios if the carbonaceous grains are the source of carbon.

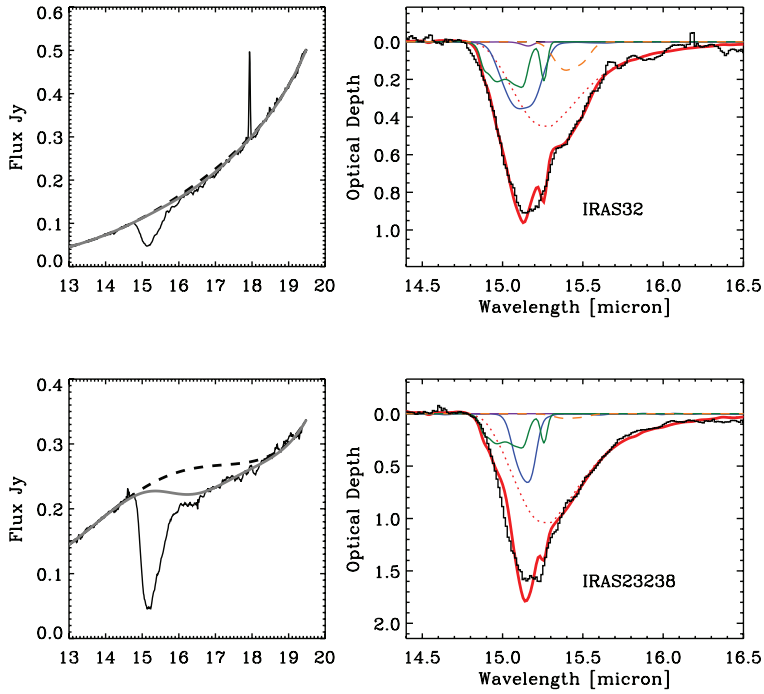

FIG. 4—*Continued*

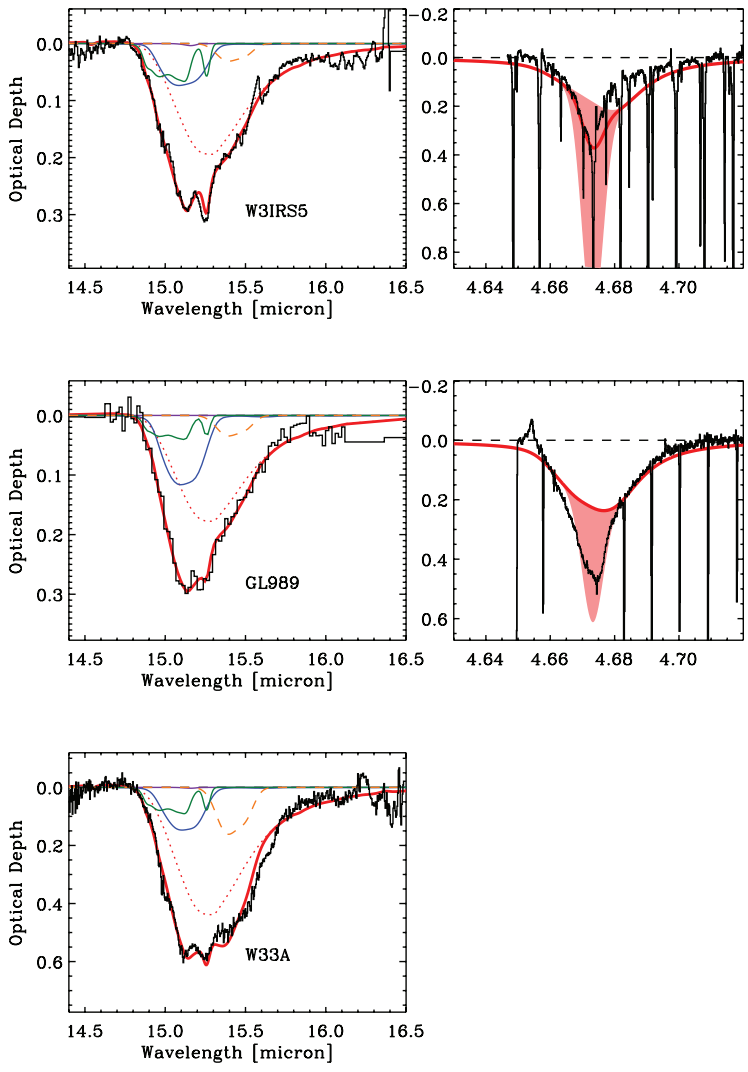

FIG. 5.—Same as Fig. 4, but for archival *ISO* spectra of massive young stars from Gerakines et al. (1999).

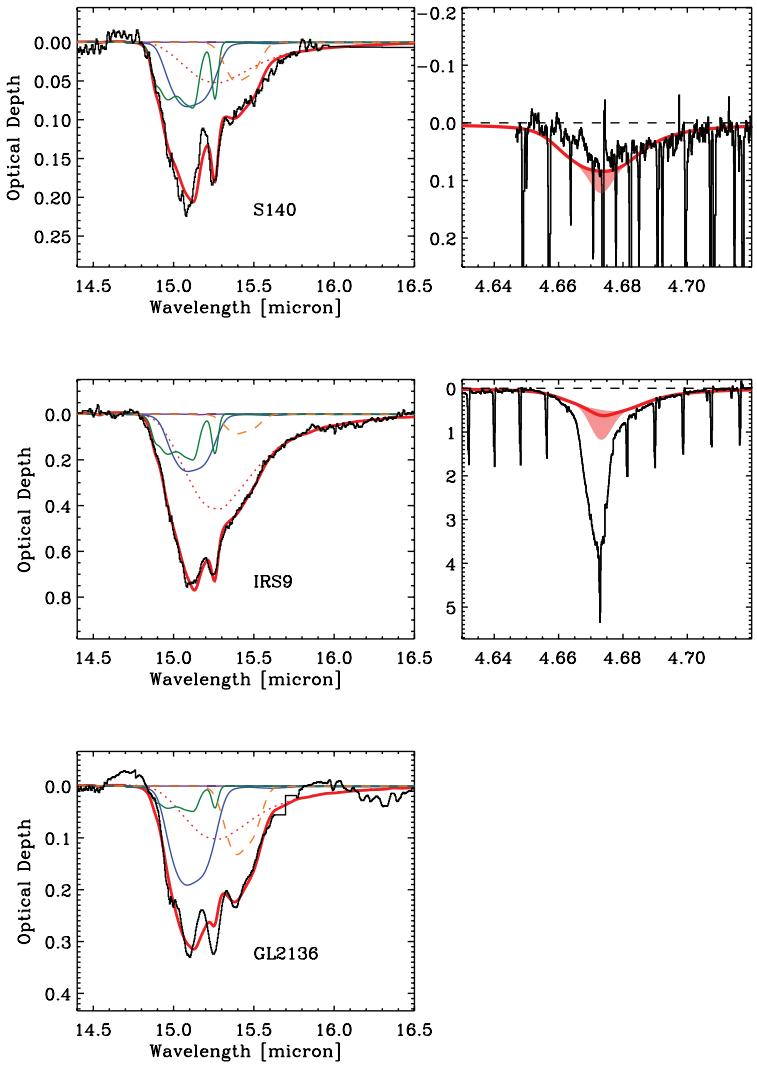

FIG. 5—*Continued*

In the following, it is explored how the data presented here can help constrain the formation and evolution of CO_2 in the interstellar medium and in protostellar envelopes in particular.

6.2. *Formation of the* CO_2:CO *System*

Having established its existence, how can the presence of large amounts of CO_2 within the CO-dominated mantle be explained? Is there a connection with the freezeout of CO at densities higher than 10^5 cm^{-3}? There is evidence from laboratory experiments that CO and CO_2 do not mix on warm-up of separately deposited layers (van Broekhuizen et al. 2006), and the possibility that the CO_2 is formed directly as part of the CO mantle using the carbon of the CO accreted from the gas phase is therefore explored. While a thick mantle of CO ice certainly offers a significant reservoir of carbon and oxygen for the formation of CO_2, the breaking of the CO triple bond to form CO_2 directly from CO requires a significant energy input. The most direct way of providing a high input of energy in dense molecular clouds is via cosmic rays. The cosmic rays can hit the grains directly but are also the dominant source of UV photons through their interaction with hydrogen molecules. A number of laboratory experiments have been performed simulating and comparing the formation of CO_2 from a pure CO ice through UV and cosmic-ray irradiation (Gerakines & Moore 2001; Loeffler et al. 2005; Jamieson et al. 2006). Jamieson et al. (2006) showed that CO_2 can be formed from a pure CO ice layer during irradiation with a 5 keV electron beam simulating heavier and more energetic cosmic rays. The experiment converted 0.49% of the CO to CO_2 with a deposited energy of 5.8×10^{16} MeV cm^{-3}, or 3.4 eV molecule^{-1}, assuming a CO ice density of 0.8 g cm^{-3}.

This value can be put into the context of dense molecular clouds by estimating the timescale for depositing the same amount of energy to a CO ice mantle with a standard cosmic-ray field. Following the approach of Shen et al. (2004), the total deposited energy by the cosmic-ray field per CO molecule per second is

$$E_{\rm dep}({\rm CR}) = \frac{m_{\rm CO}}{\rho_{\rm CO}} \sum_Z 4\pi \int_{E_{\rm min}(Z)}^{E_{\rm max}} \frac{dQ}{ds} \frac{dn}{dE} f_Z \, dE, \qquad (5)$$

where $m_{\rm CO}$ is the mass of a CO molecule and $\rho_{\rm CO}$ is the density of CO ice. Parameter dQ/ds is the energy loss as the cosmic ray traverses a length, ds, through the CO ice; dn/dE is the cosmic-ray flux spectrum; and finally, f_Z is the fraction of the energy deposited that actually remains with the grain, the rest being ejected in highly energetic electrons. Leger et al. (1985) estimate that $f_Z \sim 0.6$. The minimum cosmic-ray energy, $E_{\rm min}$, is determined

TABLE 4

ICE COLUMN DENSITIES OF THE CO_2 COMPONENTS

Source	Total CO_2	$CO_2:H_2O$	$CO_2:CO \sim 1:1$	$CO_2:CO \sim 1:25$	Pure CO_2	Shoulder	$CO:CO_2$ Ratio	χ^2	H_2O[a]
W3 IRS 5	6.56 ± 0.20	4.41 ± 0.25	0.93 ± 0.20	0.02 ± 0.08	0.83 ± 0.12	0.27 ± 0.02	0.82 ± 0.052	0.49	56.5 ± 6.0
L1448 IRS 1	2.14 ± 0.06	1.46 ± 0.11	0.32 ± 0.10	0.06 ± 0.03	0.19 ± 0.06	0.09 ± 0.01	>1.00	1.41	4.7 ± 1.6
L1448 NA	40.92 ± 0.35	32.76 ± 0.46	3.79 ± 0.23	0.00 ± 0.01	4.21 ± 0.12	0.43 ± 0.01	<0.16	1.82	...
L1455 SMM 1	63.48 ± 4.43	45.63 ± 1.78	5.72 ± 1.68	0.17 ± 1.06	7.96 ± 0.49	1.57 ± 0.05	<0.16	0.45	182.0 ± 28.2
RNO 15	2.57 ± 0.05	2.10 ± 0.08	0.43 ± 0.04	0.02 ± 0.02	0.00 ± 0.05	0.01 ± 0.05	>1.00	1.25	6.9 ± 0.6
IRAS 03254	8.86 ± 0.10	4.63 ± 0.18	2.09 ± 0.12	0.00 ± 0.01	1.51 ± 0.09	0.55 ± 0.01	0.62 ± 0.030	1.32	40.5 ± 3.7
IRAS 03271	15.37 ± 0.09	10.65 ± 0.16	2.56 ± 0.11	0.04 ± 0.07	1.68 ± 0.06	0.52 ± 0.01	0.41 ± 0.012	2.11	76.9 ± 17.6
B1-a	20.85 ± 0.14	14.23 ± 0.25	4.25 ± 0.19	0.31 ± 0.10	1.66 ± 0.11	0.37 ± 0.01	0.65 ± 0.009	1.31	104.0 ± 23.0
B1-c	84.55 ± 15.70	68.10 ± 3.72	13.95 ± 2.02	0.00 ± 1.37	0.00 ± 0.10	2.50 ± 0.11	>1.00	0.35	296.0 ± 57.0
IRAS 03439	3.32 ± 0.06	2.23 ± 0.11	0.55 ± 0.09	0.00 ± 0.03	0.37 ± 0.06	0.17 ± 0.01	0.76 ± 0.082	1.63	10.1 ± 0.9
IRAS 03445	7.07 ± 0.09	5.31 ± 0.17	1.75 ± 0.12	0.00 ± 0.06	0.00 ± 0.07	0.02 ± 0.07	0.52 ± 0.018	1.12	22.6 ± 2.8
L1489	16.20 ± 0.09	11.40 ± 0.16	1.80 ± 0.12	0.00 ± 0.07	2.66 ± 0.07	0.04 ± 0.07	0.44 ± 0.036	1.95	47.0 ± 2.8
DG Tau B	5.40 ± 0.06	3.64 ± 0.11	1.09 ± 0.09	0.00 ± 0.01	0.56 ± 0.06	0.12 ± 0.07	>1.00	0.86	26.3 ± 2.6
GL 989	6.11 ± 0.07	3.97 ± 0.19	1.37 ± 0.13	0.00 ± 0.04	0.51 ± 0.09	0.30 ± 0.02	0.64 ± 0.013	2.53	23.2 ± 1.1
HH 46	21.58 ± 0.11	16.99 ± 0.20	2.25 ± 0.12	0.00 ± 0.09	1.90 ± 0.06	0.49 ± 0.01	0.37 ± 0.016	1.34	77.9 ± 7.3
CED 110 IRS 4	12.26 ± 0.12	8.34 ± 0.22	2.10 ± 0.17	0.01 ± 0.09	1.49 ± 0.10	0.29 ± 0.02	0.56 ± 0.009	1.17	...
CED 110 IRS 6	14.30 ± 0.08	11.49 ± 0.14	1.92 ± 0.08	0.01 ± 0.07	0.78 ± 0.04	0.07 ± 0.04	0.28 ± 0.005	1.90	47.0 ± 6.0
B35	4.90 ± 0.15	3.48 ± 0.27	0.38 ± 0.20	0.09 ± 0.09	0.56 ± 0.14	0.37 ± 0.02	0.70 ± 0.223	1.29	...
IRAS 12553	5.98 ± 0.09	4.84 ± 0.16	1.07 ± 0.11	0.00 ± 0.05	0.04 ± 0.07	0.04 ± 0.07	0.63 ± 0.014	0.59	29.8 ± 5.6
ISO ChaII 54	1.81 ± 0.13	0.50 ± 0.25	0.96 ± 0.21	0.17 ± 0.07	0.16 ± 0.13	0.22 ± 0.03	>1.00	1.23	...
IRAS 13546	8.72 ± 0.12	6.22 ± 0.21	2.00 ± 0.16	0.01 ± 0.09	0.30 ± 0.09	0.08 ± 0.01	0.54 ± 0.008	0.86	20.7 ± 2.0
IRAS 15398	52.16 ± 0.79	38.83 ± 0.90	0.29 ± 0.67	1.85 ± 0.59	10.58 ± 0.29	0.80 ± 0.02	0.16 ± 0.000	1.34	148.0 ± 39.5
GSS 30 IRS 1	3.28 ± 0.06	1.86 ± 0.10	0.70 ± 0.07	0.00 ± 0.05	0.61 ± 0.05	0.09 ± 0.05	0.77 ± 0.078	1.04	15.3 ± 3.0
WL 12	4.34 ± 0.05	2.72 ± 0.10	1.36 ± 0.08	0.04 ± 0.03	0.03 ± 0.05	0.20 ± 0.05	>1.00	1.28	22.1 ± 3.0
GY 224	2.69 ± 0.09	1.90 ± 0.17	0.66 ± 0.12	0.00 ± 0.01	0.03 ± 0.09	0.15 ± 0.04	0.65 ± 0.057	1.28	...
WL 20S	5.02 ± 0.06	3.86 ± 0.11	0.75 ± 0.08	0.00 ± 0.02	0.28 ± 0.05	0.11 ± 0.05	0.64 ± 0.038	0.95	...
IRS 37	4.05 ± 0.08	2.99 ± 0.14	0.99 ± 0.12	0.00 ± 0.05	0.01 ± 0.07	0.01 ± 0.05	0.65 ± 0.012	0.85	36.5 ± 5.0
IRS 42	4.49 ± 0.05	3.39 ± 0.11	1.01 ± 0.09	0.07 ± 0.03	0.01 ± 0.05	0.09 ± 0.05	>1.00	1.01	19.5 ± 2.0
WL 6	9.33 ± 0.08	6.86 ± 0.15	2.17 ± 0.10	0.00 ± 0.06	0.12 ± 0.06	0.18 ± 0.05	0.49 ± 0.007	0.87	41.7 ± 6.0
CRBR 2422.8−3423	10.54 ± 0.06	7.30 ± 0.11	2.85 ± 0.07	0.09 ± 0.04	0.02 ± 0.04	0.36 ± 0.05	0.48 ± 0.003	1.52	45.0 ± 5.0
IRS 43	12.26 ± 0.12	8.11 ± 0.23	1.91 ± 0.16	0.00 ± 0.09	1.71 ± 0.10	0.51 ± 0.01	0.53 ± 0.047	0.84	31.5 ± 4.0
IRS 44	6.92 ± 0.08	5.01 ± 0.14	1.10 ± 0.11	0.00 ± 0.01	0.50 ± 0.08	0.34 ± 0.01	0.87 ± 0.040	1.17	34.0 ± 4.0
Elias 32	4.87 ± 0.09	2.89 ± 0.15	1.38 ± 0.12	0.07 ± 0.05	0.55 ± 0.07	0.16 ± 0.01	0.62 ± 0.015	2.21	17.9 ± 2.6
IRS 46	2.35 ± 0.12	1.64 ± 0.23	0.43 ± 0.20	0.02 ± 0.07	0.09 ± 0.12	0.09 ± 0.08	>1.00	0.20	12.8 ± 2.0
VSSG 17	5.86 ± 0.11	3.46 ± 0.19	2.20 ± 0.14	0.00 ± 0.07	0.01 ± 0.09	0.27 ± 0.03	0.53 ± 0.009	0.64	17.0 ± 2.5
IRS 51	9.32 ± 0.07	5.44 ± 0.12	3.30 ± 0.09	0.27 ± 0.05	0.07 ± 0.05	0.26 ± 0.05	0.54 ± 0.005	0.88	22.1 ± 3.0
IRS 63	6.84 ± 0.05	4.49 ± 0.10	2.26 ± 0.05	0.01 ± 0.04	0.00 ± 0.05	0.17 ± 0.05	0.51 ± 0.014	1.20	20.4 ± 3.0
L1689 IRS 5	3.37 ± 0.10	2.19 ± 0.17	1.05 ± 0.12	0.00 ± 0.06	0.00 ± 0.08	0.22 ± 0.01	0.58 ± 0.015	1.26	...
RNO 91	11.66 ± 0.16	5.94 ± 0.28	2.37 ± 0.20	0.00 ± 0.03	2.70 ± 0.14	0.62 ± 0.02	0.64 ± 0.026	1.49	39.0 ± 5.0
W33A	14.11 ± 0.29	9.96 ± 0.30	1.70 ± 0.22	0.02 ± 0.11	1.13 ± 0.13	1.41 ± 0.11	0.59 ± 0.025	1.00	113.0 ± 28.3
GL 2136	6.25 ± 0.20	2.30 ± 0.20	2.40 ± 0.10	0.00 ± 0.10	0.61 ± 0.10	1.15 ± 0.16	0.77 ± 0.02	0.67	47.2 ± 4.7
S68N	43.27 ± 16.54	30.99 ± 0.75	5.38 ± 1.18	0.09 ± 1.01	6.81 ± 0.38	0.00 ± 0.50	<0.16	1.90	...
EC 74	2.89 ± 0.08	2.00 ± 0.14	0.79 ± 0.07	0.00 ± 0.05	0.00 ± 0.01	0.19 ± 0.01	0.44 ± 0.032	1.90	10.7 ± 1.8
EC 82	2.54 ± 0.04	1.88 ± 0.08	0.07 ± 0.07	0.12 ± 0.02	0.34 ± 0.04	0.08 ± 0.05	>1.00	2.18	3.9 ± 0.7
SVS 4-5	17.21 ± 0.10	12.37 ± 0.18	3.48 ± 0.13	0.00 ± 0.08	0.68 ± 0.07	0.73 ± 0.02	0.43 ± 0.009	1.14	56.5 ± 11.3
EC 90	5.44 ± 0.05	3.53 ± 0.09	1.67 ± 0.07	0.12 ± 0.03	0.01 ± 0.05	0.17 ± 0.02	0.81 ± 0.011	1.39	16.9 ± 1.6
SVS 4-10	8.25 ± 0.05	5.37 ± 0.09	2.35 ± 0.07	0.07 ± 0.04	0.12 ± 0.04	0.35 ± 0.01	0.57 ± 0.004	1.51	16.0 ± 1.4
CK 4	1.98 ± 0.09	1.20 ± 0.16	0.62 ± 0.08	0.00 ± 0.05	0.00 ± 0.05	0.15 ± 0.00	0.75 ± 0.099	1.00	15.6 ± 15.6
CK 2	11.93 ± 0.21	9.02 ± 0.38	2.29 ± 0.23	0.01 ± 0.16	0.26 ± 0.15	0.31 ± 0.01	0.32 ± 0.030	0.75	35.7 ± 3.5
RCRA IRS 5	14.28 ± 0.13	8.38 ± 0.23	4.52 ± 0.17	0.01 ± 0.10	0.80 ± 0.10	0.68 ± 0.02	0.58 ± 0.005	1.86	37.6 ± 2.8
RCRA IRS 7A	19.64 ± 0.12	13.17 ± 0.21	3.89 ± 0.16	0.00 ± 0.09	2.15 ± 0.08	0.52 ± 0.01	0.58 ± 0.006	1.20	109.0 ± 19.2
RCRA IRS 7B	26.74 ± 0.22	19.02 ± 0.35	2.38 ± 0.24	0.00 ± 0.25	4.94 ± 0.11	0.36 ± 0.10	<0.16	2.26	110.0 ± 19.7
IRAS 32	18.70 ± 0.21	10.21 ± 0.36	4.00 ± 0.28	0.13 ± 0.16	3.04 ± 0.16	1.32 ± 0.12	0.56 ± 0.014	1.52	52.6 ± 18.8
S140	3.78 ± 0.07	1.17 ± 0.10	1.06 ± 0.07	0.00 ± 0.00	1.06 ± 0.04	0.44 ± 0.13	0.85 ± 0.024	1.25	19.3 ± 1.9
NGC 7538 IRS 9	15.81 ± 0.13	9.41 ± 0.15	3.03 ± 0.12	0.01 ± 0.06	2.51 ± 0.08	0.75 ± 0.97	0.67 ± 0.009	0.89	64.1 ± 6.4
IRAS 23238	32.51 ± 0.30	23.66 ± 0.42	4.20 ± 0.20	0.00 ± 0.02	4.10 ± 0.13	0.40 ± 0.01	<0.16	3.02	130.0 ± 22.6

NOTES.—All column densities are in 10^{17} cm^{-2}. All uncertainties are statistical and do not include systematic uncertainties from, e.g., the continuum determination.

[a] For consistency, the new water ice column densities from Paper I are used, where available. They are generally consistent with the few published values measured on the same, or similar, data sets, but with a few values differing by 15%–20%.

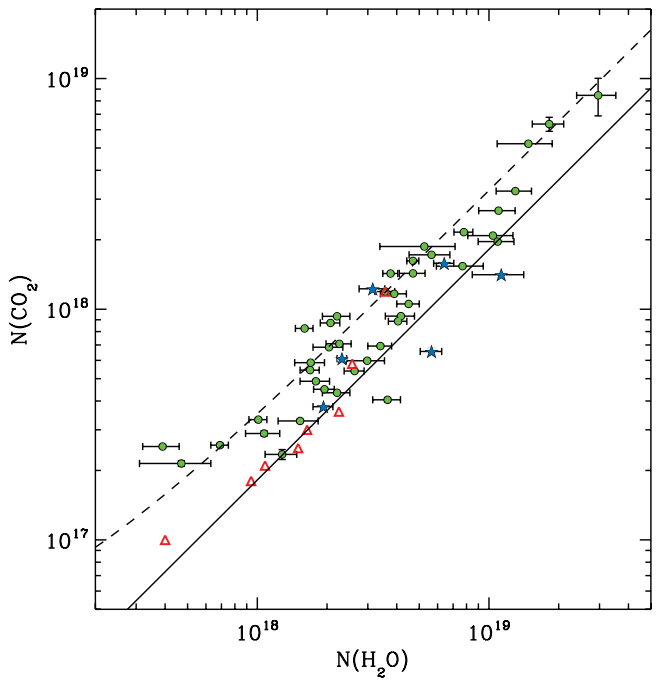

FIG. 6.—Relation between H_2O ice column density and CO_2 ice column density. The green filled circles are low-mass stars with luminosities of 0.1–100 $L_\odot$, while the blue filled stars indicate the massive YSOs from the *ISO* sample with luminosities of $L = 10^4$–10^5 $L_\odot$. The red open triangles are the background stars in Taurus from Whittet et al. (2007), as well as CK 2 from Knez et al. (2005). The dashed line is a linear least-squares fit to the low-mass stars. The solid line is the linear fit to the background stars.

by the various factors that may drain energy from the particles. These include interactions with dust grains, with the molecular gas itself, as well as drag from magnetic fields. The importance of these effects depends sensitively on Z, as well as the cosmic-ray energy. Leger et al. (1985) showed that interactions with the

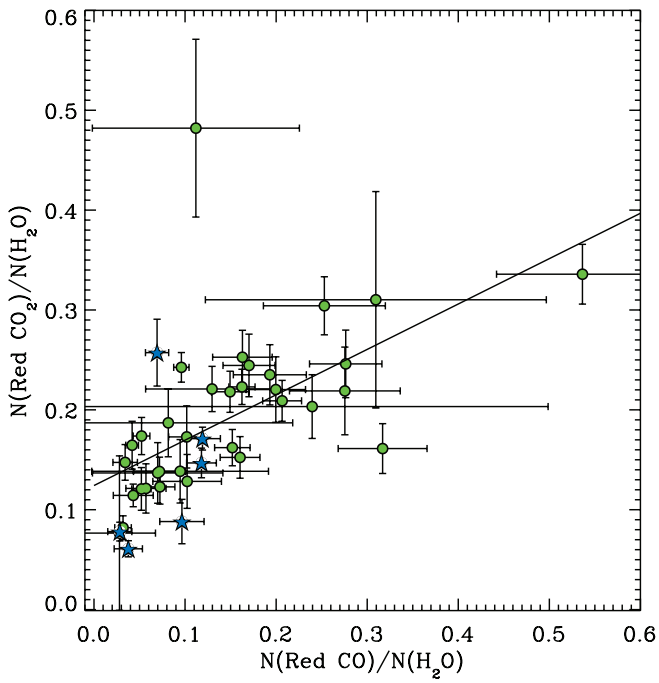

FIG. 7.—Correlation between the CO_2 : H_2O component and the red CO component (CO : H_2O) from Pontoppidan et al. (2003b). The green filled circles are the low-mass stars, while the blue filled stars are the high-mass YSOs observed with *ISO*. The solid line is a linear fit to the low-mass YSOs.

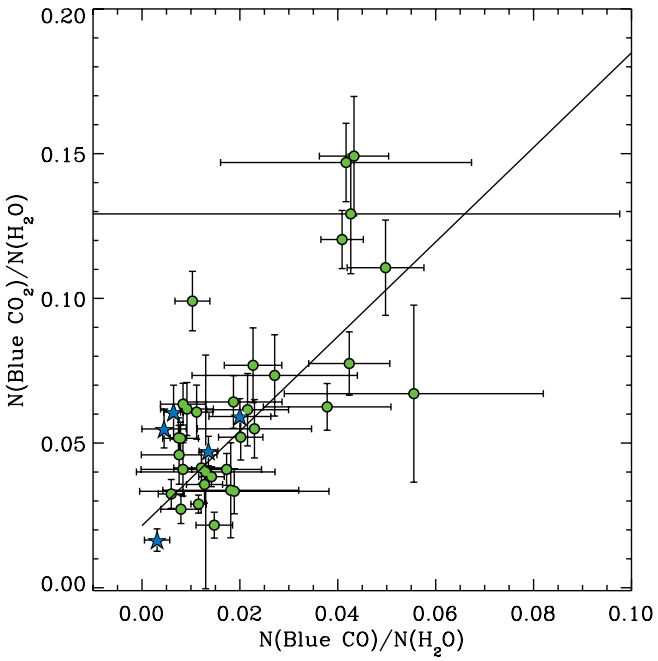

FIG. 8.—Same as Fig. 7, but for the correlation between the blue CO_2 component abundance and the blue CO component abundance from Pontoppidan et al. (2003b).

gas only affect the cosmic-ray spectrum at $A_V > 50$ mag. However, dust can effectively stop low-energy (<100 MeV for iron) cosmic rays at $A_V < 10$ mag, and that determines $E_{\rm min}$.

For these assumptions, the energy deposited by cosmic rays in a CO ice mantle is 8×10^{-14} eV molecule^{-1} s^{-1}, which means that the Jamieson et al. (2006) experiment corresponds to roughly 350 yr of cosmic-ray irradiation or, assuming a constant rate of CO_2 formation, $\sim 3.5 \times 10^4$ yr to convert 50% of the CO mantle to CO_2. Although the input cosmic-ray flux spectrum is very

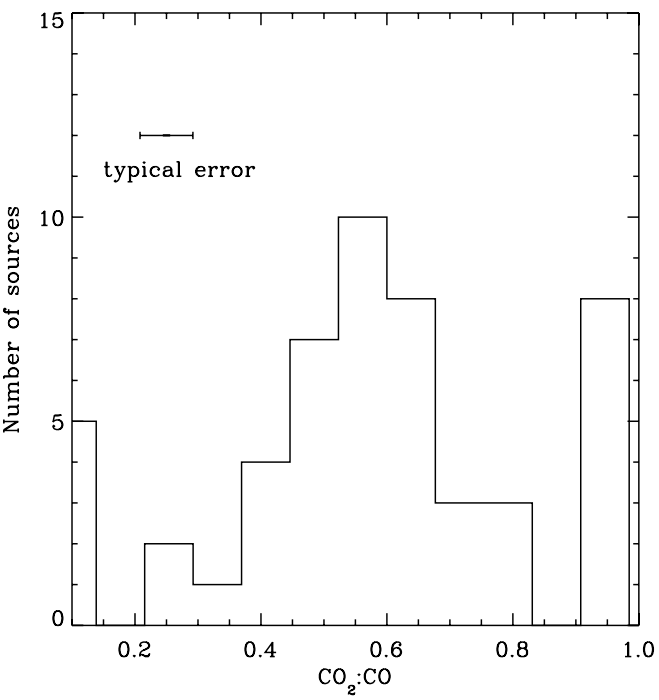

FIG. 9.—Distribution of CO_2 : CO mixing ratios as determined from the CO_2 blue component profile fit.

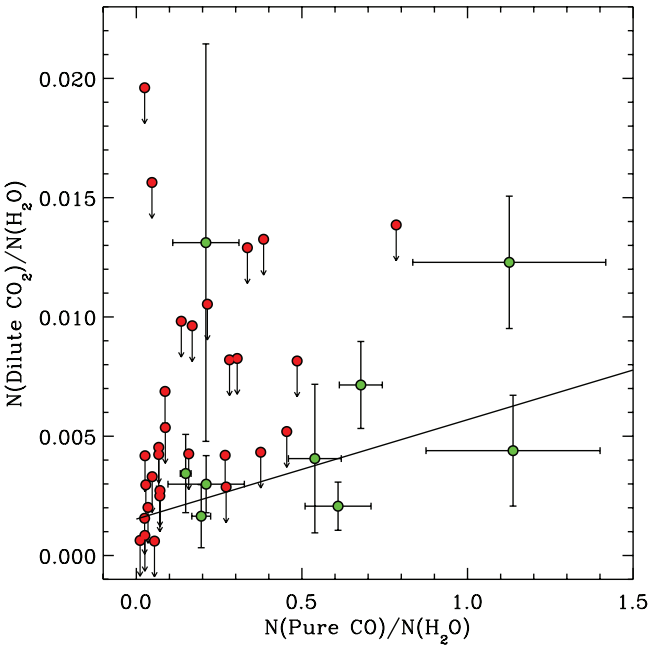

FIG. 10.—Relation between the dilute CO_2 component abundance and the middle (pure) CO component abundance from Pontoppidan et al. (2003b). The green filled circles are detections, while the red filled circles indicate upper limits on the dilute CO_2 component. The solid line is a linear fit to the detections.

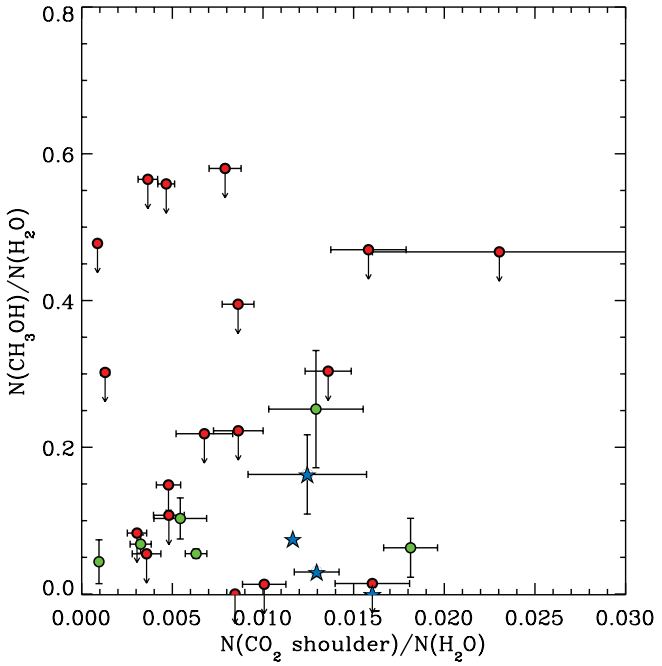

FIG. 11.—Relation between the abundance of the CO_2 "shoulder" component and the CH_3OH abundance from Paper I.

uncertain, especially at low energies, the conclusion is that it is plausible that cosmic rays can provide the necessary energy input to form the observed CO_2:CO component.

In this context, what is the implication of the presence of the dilute component discussed in § 5.3.2? One possibility is that the CO ice with a low concentration of CO_2 is younger than the CO_2:CO $\sim$ 1:1 component. This would happen if the conversion of CO to CO_2 occurs at a constant rate.

Jamieson et al. (2006) predict the presence of a range of carbon oxide species in addition to CO_2, of which the most abundant is C_3O_2. The quality of the *Spitzer* IRS spectra allows a sensitive search for this molecule in the solid state through its modes at $\sim$18.5 μm, yet it is not clearly detected in any of the spectra presented here (see § 5.5).

6.3. CO_2 *as a Temperature Tracer*

CO_2 has been suggested to be a tracer of strong heating based on simulated annealing experiments in the laboratory to 100 K (Gerakines et al. 1999). The proposed mechanism is that the CO_2 segregates out of the hydrogen-bonding mixture with water and possibly CH_3OH to produce inclusions of pure CO_2. These inclusions in turn produce the characteristic double peak observed in many high-mass YSOs. While the very high temperatures required for the segregation process in a laboratory setting probably correspond to somewhat lower temperatures on astronomical timescales, they are still well above the temperatures of 10–40 K that dominate the column densities through protostellar envelopes around low-mass stars. Thus, it seems surprising that many of the surveyed low-mass stars show a double peak. The decomposition and visual inspection of the spectra reveal that a pure CO_2 component is clearly detected in 18 of the 48 low-mass stars, or almost 40%.

At least one other mechanism to produce a pure CO_2 ice component exists. The existence of a ubiquitous CO_2:CO component has been suggested before and is strengthened by the sample presented here. This component may also produce pure CO_2 through distillation. On warm-up of a CO_2:CO mixture the CO will desorb, leaving the CO_2 behind, but will do so at much lower temperatures (20–30 K; van Broekhuizen et al. 2006). This is consistent with the anticorrelation between the abundances of pure CO and pure CO_2 shown in Figure 12.

One way of distinguishing this process with the formation of pure CO_2 via segregation is to calculate the fraction, P, of thermally processed icy material at temperatures above a certain critical temperature, $T_{\rm crit}$, along a given line of sight through a protostellar envelope. Clearly, $T_{\rm crit}$ is expected to be much lower for the distillation process than for the segregation process. Assuming that T is a monotonically decreasing function of radius, P is given by

$$P = \frac{\int_{R_{\rm crit}}^{R_{\rm sub}} n_{\rm CO_2}(r)\, dr}{\int_{\infty}^{R_{\rm sub}} n_{\rm CO_2}(r)\, dr}, \tag{6}$$

where $R_{\rm crit}$ is the radius where $T = T_{\rm crit}$ and $R_{\rm sub}$ is the radius where the processed CO_2 ice sublimates. Parameter $n_{\rm CO_2}$ is the density of the CO_2 component that is transformed to pure, crystalline CO_2 on heating to $T_{\rm crit}$. The use of a critical temperature assumes that the process forming pure CO_2 is a thermal process governed by some activation energy and described by an Arrhenius relation.

The first step is to estimate the value of $T_{\rm crit}$ for the segregation process in water-rich ice. Because of the long timescales and low pressures in the interstellar medium compared to the short timescales and high pressures of a laboratory experiment, it is not appropriate to apply the critical temperatures from the laboratory directly to an astrophysical problem. For a process not dependent on pressure, such as the segregation of CO_2 from a water matrix, the critical temperatures in the two settings are related via

$$\frac{\tau_{\rm astro}}{\tau_{\rm lab}} = \exp\left[E_a\left(\frac{1}{T_{\rm astro}} - \frac{1}{T_{\rm lab}}\right)\right], \tag{7}$$

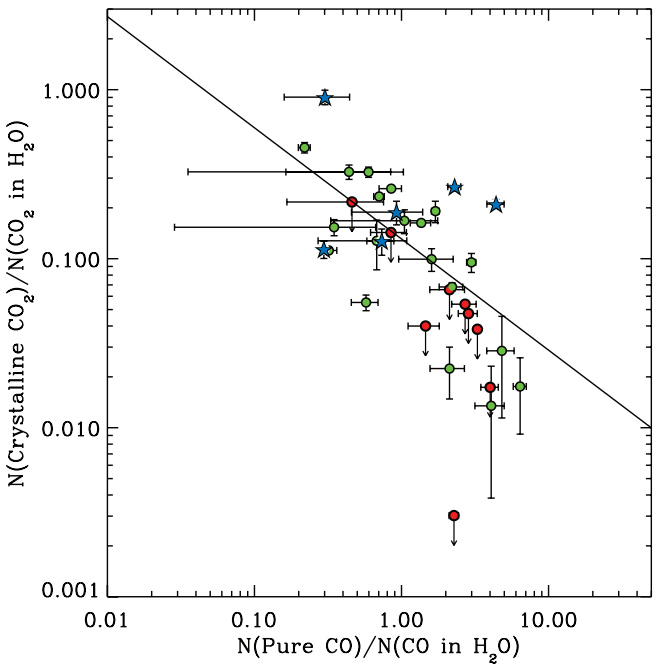

FIG. 12.—Relation between the CO and CO_2 temperature tracers. The CO_2 temperature tracer is the ratio of the column density in the double-peaked, pure CO_2 component relative to CO_2 in water. The CO temperature tracer is the amount of pure CO relative to CO trapped in water ice. Green filled circles are low-mass YSOs, blue filled stars are high-mass YSOs, and red filled circles are upper limits on the CO_2 temperature tracer. The solid line is a fit to the low-mass YSOs.

where E_a is the activation energy in kelvin, while $\tau_{\rm astro}$ and $\tau_{\rm lab}$ are the *e*-folding timescales of a given process in the interstellar medium and in the laboratory, respectively. Because E_a is unknown, measurements of the laboratory timescale at two different temperatures are required.

Unfortunately, the kinetics of the segregation process are not well known. From the experiment of Ehrenfreund et al. (1999) a rough estimate can be made of $\tau_{\rm lab} \sim 1$ hr at 100 K and $\tau_{\rm lab} \sim 1$ minute at 120 K. However, they use a tertiary $CO_2:H_2O:CH_3OH = 1:1:1$ mixture, which has a concentration of methanol much higher than that found in typical low-mass protostellar envelopes. Conversely, recent experiments with a binary $CO_2:H_2O = 1:4$ mixture by Öberg et al. (2007a) show that the CO_2 bending mode double peak has formed already at 75 K on laboratory timescales of hours. Using a timescale of 10^5 yr, a typical time for the collapse front to reach the outer boundary of the protostellar core, the Ehrenfreund et al. (1999) values give $E_a \sim 4900$ K and $T_{\rm crit} \equiv T_{\rm astro} \sim 70$ K. Boogert et al. (2000) find $E_a = 4900$ and $T_{\rm crit} = 77$ K with similar assumptions. If it is instead assumed that $T_{\rm lab} = 75$ K for an *e*-folding timescale of 1 hr, as indicated by Öberg et al. (2007a), but the activation energy of 4900 K is retained, $T_{\rm crit} \sim 57$ K. It is stressed that these values for $T_{\rm crit}$ are educated guesses at best and that quantitative kinetic laboratory experiments are needed to measure the actual value. In conclusion, $T_{\rm crit}$ is taken in the range 60–80 K.

It is also important to note that the time a dust grain can be expected to spend at temperatures between, say, 70 and 90 K is much less than 10^5 yr. In the simplest physical one-dimensional model of an infalling envelope (Shu 1977), a dust grain at the radii corresponding to such temperatures will be in free fall. The timescale for it passing through this region for a typical 1 $M_\odot$ young star is 75 yr, which in turn will increase $T_{\rm crit}$ for segregation to 78 K for the CH_3OH-rich mixture. Using a two-dimensional infall model that takes rotation into account will likely increase the infall timescale somewhat. The confidence of the value of $T_{\rm crit}$ can obviously be improved significantly with a quantitative laboratory simulation coupled with a more detailed infall model.

A value for the desorption temperature, $T_{\rm sub}$, of the pure, crystalline CO_2 component formed by the segregation process is also needed. It is reasonable to expect the segregated CO_2 to be in the form of inclusions embedded in the water ice. The question is whether the CO_2 is trapped in the water or will be able to escape at temperatures lower than the interstellar water ice desorption temperature of 110 K (Fraser et al. 2001). While the Ehrenfreund experiments retain the CO_2 inclusions until the water ice desorbs at 150 K, the Öberg et al. (2007a) experiments find that the bulk of the CO_2 ice desorbs at

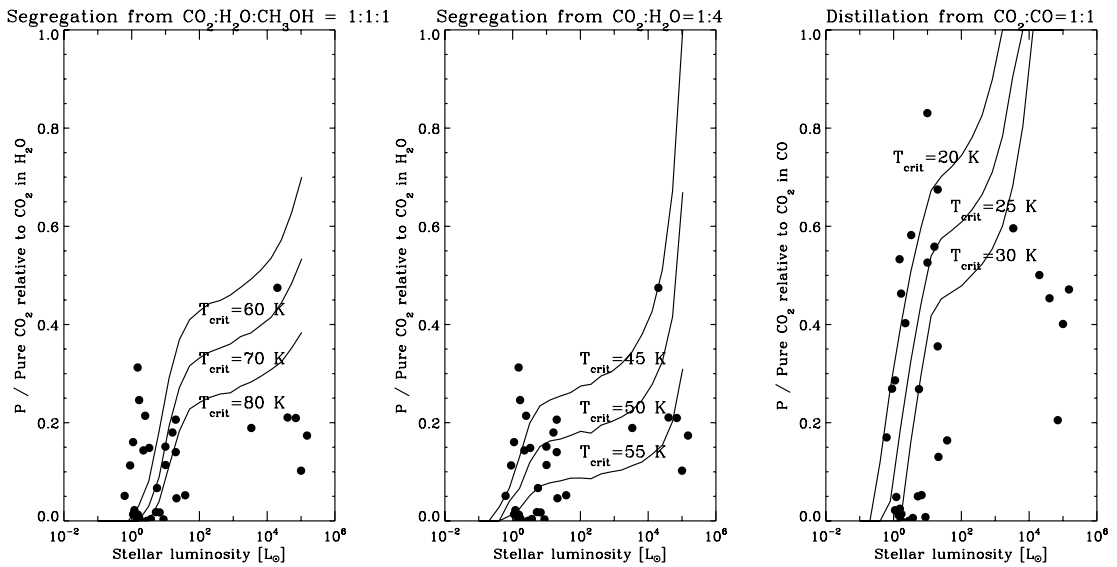

FIG. 13.—Fraction of pure CO_2 compared to models for different critical temperatures relevant for segregation (*left*) and CO desorption (*right*). In the models in the left and middle panels, an inner edge at 100 AU is used, while the models in the right panel fit better with an inner edge at 300 AU. The filled circles are the observed values for the subset of our sample that have measured luminosities from Berrilli et al. (1989), Ladd et al. (1993), Chen et al. (1995), Saraceno et al. (1996), Bontemps et al. (2001), Larsson et al. (2000), Kaas et al. (2004), and Pontoppidan & Dullemond (2005).

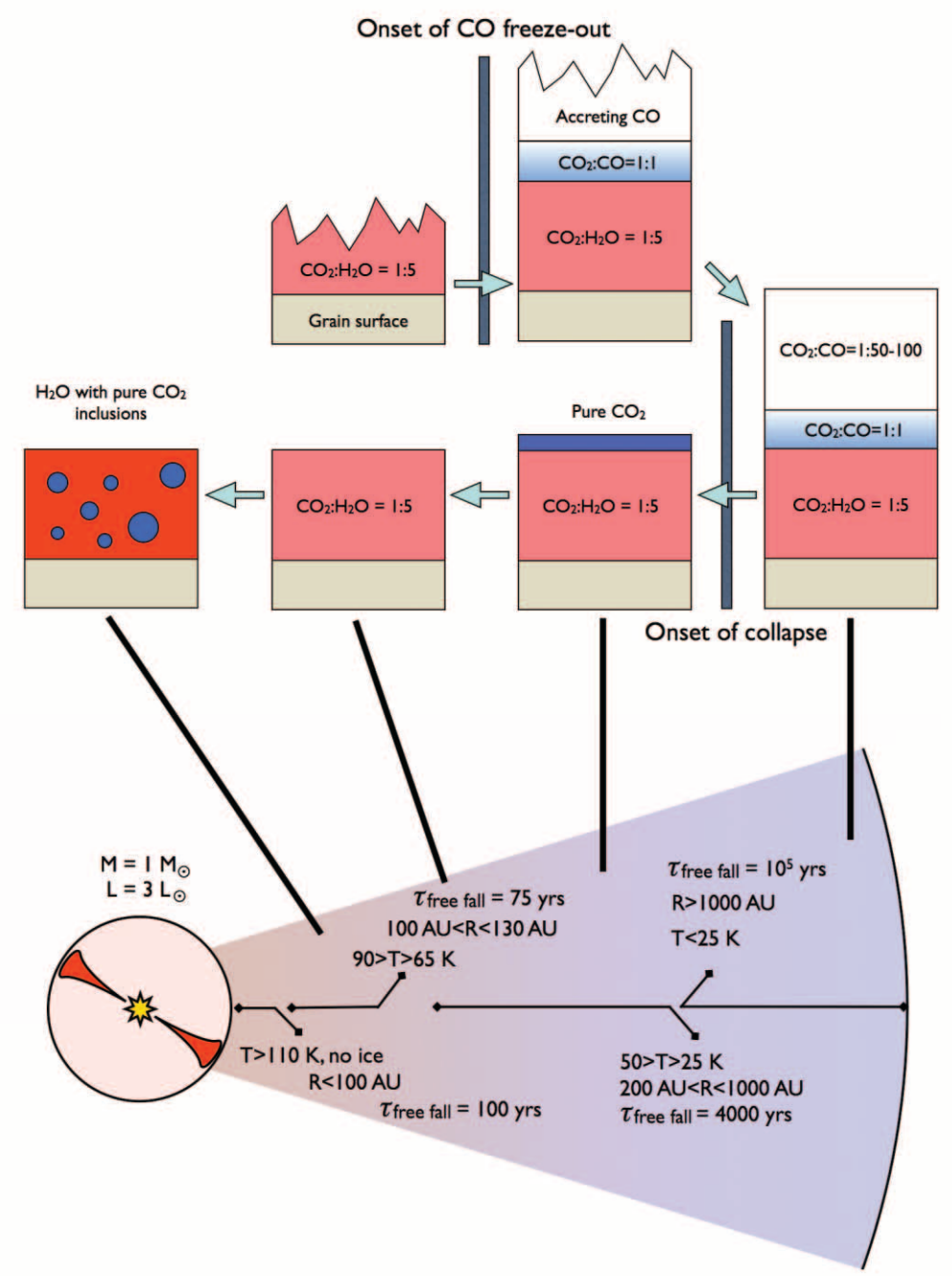

FIG. 14.—Sketch of the CO_2 ice structure in a typical low-mass protostellar envelope. The upper section of the sketch shows the suggested evolution of the $CO:CO_2:H_2O$ system on a single dust grain from the formation of the protostellar core until the grain is accreted on a protoplanetary disk surrounding the central star. The lower section indicates where in a collapsing envelope the various stages of ice mantle evolution can be found.

temperatures much lower than the water ice. This is consistent with the result of Collings et al. (2004), who classified CO_2 as a molecule that is not easily trapped in a water ice matrix. The fact that the tertiary mixture Ehrenfreund experiment appears to retain the CO_2 to higher temperatures than the binary H_2O mixtures may be related to the CH_3OH changing the trapping properties of the matrix. In any case, to match the different experiments, an interstellar CO_2 desorption temperature of 110 K is assumed for the Ehrenfreund experiment, 60 K for the Öberg experiment, and 50 K for the pure CO_2 layer produced by the distillation process of $CO_2:CO$. The physical interpretation is that the methanol-rich ice traps the CO_2 ice until the water desorbs. The water-rich binary mixture only traps CO_2 to temperatures slightly higher than the desorption temperature of pure CO_2 in accordance with Collings et al. (2004), while the $CO_2:CO$ mixture obviously does not trap CO_2 at all.

The next step is to choose a radial temperature and density structure that can be used to calculate P. While P is sensitive to a range of structural parameters for the envelope, the dominant one is the luminosity of the central source. It is beyond the scope of this paper to explore the parameter space of the structures of protostellar envelopes, but it is instructive to construct an example. For simplicity a static, one-dimensional power-law envelope [$\rho(R) \propto (R/R_0)^{-1.5}$] with A_V of 50 mag and

$R_0 = 100$–300 AU is assumed. Furthermore, it is assumed that the envelope is empty within R_0. This is actually an envelope structure that favors a large P. More evolved envelopes dominated by infalling material to large radii will have a shallower density profile and thus more of the line-of-sight column density at larger radii. In this sense, the model P curves are upper limits. The dust temperature is calculated using the Monte Carlo code RADMC (Dullemond & Dominik 2004) coupled with a dust opacity constructed to fit the extinction curve as measured using the c2d photometric catalogs (K. Pontoppidan et al. 2008, in preparation). The resulting dust temperature at 100 AU varies from 40 to 1200 K for source luminosities of 0.1–10^5 $L_\odot$.

Figure 13 shows the observed values of P as a function of source luminosity compared to model curves for different values of $T_{\rm crit}$ under the assumptions that the pure CO_2 originates either in the CO_2:H_2O component or in the CO : CO_2 component through the processes discussed above. The P curves for both the Ehrenfreund and Öberg experiments are shown, as well as the curves expected for the formation of pure CO_2 through distillation of the CO_2:CO component.

First, it is noted that P is not necessarily a monotonic increasing function with luminosity. This is because the evaporation of the pure CO_2 ice component in the innermost regions of the envelope where $T > T_{\rm sub}$ competes with the formation of pure CO_2 at temperatures $T_{\rm crit} < T < T_{\rm sub}$. This is seen in Figure 13 as a turnover in the models as the luminosity increases. For higher power-law indices of the envelope, the P curves may even decrease with increasing luminosity.

Comparing the data points with the model curves, the results are as follows: Assuming a complete transformation of CO_2 mixed with water ice to pure CO_2 inclusions, the observed points are consistent with a critical temperature for this process of 50–70 K, depending on whether the Ehrenfreund or the Öberg experiments are considered. Conversely, assuming a conversion of CO_2 mixed with CO to pure CO_2, a critical temperature of at most 25 K explains the highest observed P-values toward low-mass stars. The measured values of P are very sensitive to the presence of cold foreground clouds contributing an unrelated column density, as well as the detailed structure of the inner envelope, in particular the arbitrary location of an inner edge at 100–300 AU. This has important consequences for the use of the CO_2 bending mode as an astrophysical tracer. For instance, the models show that the double peak should have a roughly constant relative strength for sources with luminosities between a few and at least 10^3 $L_\odot$. Therefore, if a source within that luminosity range shows no sign of a double peak, it is an indication of the presence of a significant contribution to the extinction from foreground material, unrelated to the protostellar envelope.

In conclusion, the splitting of the CO_2 bending mode toward low-mass protostars can be explained by segregation in strongly heated water-rich ices as described in Gerakines et al. (1999) only for protostellar envelopes with steep density profiles extending all the way to 100 AU from the central star, and for concentrations of CH_3OH much higher than the observed abundances. The experiments of Öberg et al. (2007a) may also explain the data for such envelopes, but $T_{\rm crit}$ is not well defined for this experiment.

The resulting distribution of CO_2 ice in the different environments is sketched in Figure 14.

7. DISCUSSION AND CONCLUSIONS

In this paper, a picture is presented in which the dominant ice components, H_2O, CO_2, CO, and, in a limited number of cases, CH_3OH, appear to constitute an intimately connected system; the observational characteristics of each species are directly affected by the presence of the others. Other molecules act as trace constituents with abundances that are too low to significantly affect the profiles of the dominant species; i.e., other species did not have to be invoked to explain the observed band profiles. This is in contrast to the very complex 5–8 μm region discussed in Paper I.

The survey has shown that the CO_2 bending mode profiles toward low-luminosity ($0.1\ L_\odot < L < 100\ L_\odot$), solar-type YSOs do not differ strongly in their basic structure from those observed toward massive, luminous YSOs ($L > 1000\ L_\odot$). All protostellar envelopes, as well as quiescent molecular clouds probed by lines of sight toward background stars, are dominated by CO_2 mixed with water with abundances of 20% relative to water ice, but with a significant additional contribution of 10% of CO_2 mixed with CO. The other components needed to explain the CO_2 bending mode are present with much smaller abundances, or a few percent each with respect to water ice.

While the CO_2:H_2O component might form from CO and OH via equation (1), it is probable that, because of the lack of residual atomic hydrogen, the CO_2:CO component forms through a different chemical route. In addition, since the band profiles indicate that the CO_2 in this component can have concentrations of anything from 2:1 to less than 1:100 relative to CO, a variable effect highly sensitive to either the environment or age of the ice must play a role. Based on observations of a sample of background stars, Bergin et al. (2005) suggest that the formation of the CO_2:CO component is related to the abundance of atomic oxygen relative to atomic hydrogen in the gas phase and predict that it forms in low-density regions of the cloud. Observationally, this would produce CO and CO_2 profiles dominated by the CO_2 : CO $\sim$ 1:1 component in low-density regions. It would also result in the CO_2:CO layer being placed below the water-rich layer on each grain. In this case, the formation of pure CO_2 by the desorption of CO as proposed here would not work.

A different scenario is suggested in which the CO_2:CO component is connected to the rapid freezeout of pure CO at higher densities. This scenario is practically independent of the gas-phase chemistry but requires a mechanism for forming CO_2 directly from CO. Such a mechanism will most likely involve a highly energetic input from cosmic rays; UV irradiation with $\lambda > 1200$ Å will not work in the absence of water (Öberg et al. 2007b). While the energy input from a standard cosmic-ray field is likely sufficient, this process would also tend to form more complex carbon oxides in the ice. While these are not detected in our *Spitzer* spectra, their absence is not strongly constraining, given that the molecular properties of their bands, such as strengths, are not well known.

It is confirmed that the CO_2 ice profile is an excellent ice temperature tracer. Comparison with the stretching vibration band of solid CO shows that the CO_2 correlates well with the ratio of pure CO to CO:H_2O, an established ice temperature tracer. The observed differences between CO_2 bending mode profiles are consistent with differences in the fraction of the sight lines that have been heated above a certain threshold temperature, $T_{\rm crit}$, to produce a double-peaked profile. More luminous YSOs have generally had a larger fraction of their ice column densities at temperatures above $T_{\rm crit}$, but the prevalence of the characteristic double peak shows that even the low-luminosity YSOs have thermally processed inner envelopes.

There are several possibilities for the value of $T_{\rm crit}$. For the massive YSOs, strong annealing of methanol-rich ices to

temperatures higher than 100 K in a laboratory setting was invoked to explain the observed abundance of pure CO_2 ice by Gerakines et al. (1999). It is suggested that this corresponds to $T_{crit} = 50-80$ K under the conditions in collapsing protostellar envelopes. These are high temperatures that put restrictions on the density structure of the protostellar envelopes in order to reproduce the observed abundances of pure CO_2. Laboratory experiments measuring the kinetics of the annealing process in methanol-poor CO_2:H_2O ice mixtures will be needed to use this process in quantitative modeling of ice mantle processing.

It is therefore argued that the presence of a significant fraction of pure CO_2 toward so many of the low-mass YSOs in the survey indicates that another, lower temperature process may play a role. Our survey, as well as others, measures a significant fraction of the CO_2 ice mixed with CO, rather than with water. This mantle component will form a layer of pure CO_2 on very moderate heating to $T_{crit} = 20$–30 K as the CO desorbs, leaving the CO_2 behind. This process has therefore the potential to create pure CO_2 by *distillation* rather than *segregation*. Note that the new observations presented here do not rule out that the segregation process is responsible for a significant fraction of the pure CO_2 in the sample of *massive* YSOs originally discussed in Gerakines et al. (1999), in particular since less CO will be frozen out in the warm envelopes surrounding massive YSOs. The simple protostellar models presented here seem to indicate that both mechanisms for producing CO_2 in general contribute to the double peak in low-mass YSOs.

Support for K. M. P. was provided by NASA through Hubble Fellowship grant 1201.01 awarded by the Space Telescope Science Institute, which is operated by the Association of Universities for Research in Astronomy, Inc., for NASA, under contract NAS 5-26555. Astrochemistry in Leiden is supported by a Spinoza grant of the Netherlands Organization for Scientific Research (NWO). Support for this work, part of the *Spitzer Space Telescope* Legacy Science Program, was provided by NASA through contracts 1224608 and 1230779 issued by the Jet Propulsion Laboratory, California Institute of Technology under NASA contract 1407. Some of the data presented herein were obtained at the W. M. Keck Observatory, which is operated as a scientific partnership among the California Institute of Technology, the University of California, and the National Aeronautics and Space Administration. The Observatory was made possible by the generous financial support of the W. M. Keck Foundation. The authors wish to recognize and acknowledge the very significant cultural role and reverence that the summit of Mauna Kea has always had within the indigenous Hawaiian community. We are most fortunate to have the opportunity to conduct observations from this mountain.

REFERENCES

Bergin, E. A., Langer, W. D., & Goldsmith, P. F. 1995, ApJ, 441, 222
Bergin, E. A., Melnick, G. J., Gerakines, P. A., Neufeld, D. A., & Whittet, D. C. B. 2005, ApJ, 627, L33
Berrilli, F., Ceccarelli, C., Liseau, R., Lorenzetti, D., Saraceno, P., & Spinoglio, L. 1989, MNRAS, 237, 1
Bontemps, S., et al. 2001, A&A, 372, 173
Boogert, A. C. A., Blake, G. A., & Tielens, A. G. G. M. 2002, ApJ, 577, 271
Boogert, A. C. A., et al. 2000, A&A, 353, 349
———. 2008, ApJ, 678, 985 (Paper I)
Boonman, A. M. S., van Dishoeck, E. F., Lahuis, F., & Doty, S. D. 2003, A&A, 399, 1063
Chang, Q., Cuppen, H. M., & Herbst, E. 2007, A&A, 469, 973
Chen, H., Myers, P. C., Ladd, E. F., & Wood, D. O. S. 1995, ApJ, 445, 377
Chiar, J. E., Adamson, A. J., Kerr, T. H., & Whittet, D. C. B. 1995, ApJ, 455, 234
Collings, M. P., Anderson, M. A., Chen, R., Dever, J. W., Viti, S., Williams, D. A., & McCoustra, M. R. S. 2004, MNRAS, 354, 1133
Croat, T. K., Stadermann, F. J., & Bernatowicz, T. J. 2005, ApJ, 631, 976
Dartois, E., Demyk, K., d'Hendecourt, L., & Ehrenfreund, P. 1999, A&A, 351, 1066
d'Hendecourt, L. B., Allamandola, L. J., & Greenberg, J. M. 1985, A&A, 152, 130
d'Hendecourt, L. B., Allamandola, L. J., Grim, R. J. A., & Greenberg, J. M. 1986, A&A, 158, 119
Dullemond, C. P., & Dominik, C. 2004, A&A, 417, 159
Ehrenfreund, P., Boogert, A. C. A., Gerakines, P. A., Tielens, A. G. G. M., & van Dishoeck, E. F. 1997, A&A, 328, 649
Ehrenfreund, P., et al. 1999, A&A, 350, 240
Fournier, J., Deson, J., Vermeil, C., & Pimentel, G. C. 1979, J. Chem. Phys., 70, 5726
Fraser, H. J., Collings, M. P., McCoustra, M. R. S., & Williams, D. A. 2001, MNRAS, 327, 1165
Gerakines, P. A., & Moore, M. H. 2001, Icarus, 154, 372
Gerakines, P. A., Schutte, W. A., & Ehrenfreund, P. 1996, A&A, 312, 289
Gerakines, P. A., Schutte, W. A., Greenberg, J. M., & van Dishoeck, E. F. 1995, A&A, 296, 810
Gerakines, P. A., et al. 1999, ApJ, 522, 357
Grim, R. J. A., & d'Hendecourt, L. B. 1986, A&A, 167, 161
Jamieson, C. S., Mebel, A. M., & Kaiser, R. I. 2006, ApJS, 163, 184
Kaas, A. A., et al. 2004, A&A, 421, 623
Knez, C., et al. 2005, ApJ, 635, L145
Ladd, E. F., Lada, E. A., & Myers, P. C. 1993, ApJ, 410, 168
Lahuis, F., van Dishoeck, E. F., Blake, G. A., Evans, N. J., II, Kessler-Silacci, J. E., & Pontoppidan, K. M. 2007, ApJ, 665, 492
Larsson, B., et al. 2000, A&A, 363, 253
Leger, A., Jura, M., & Omont, A. 1985, A&A, 144, 147
Lin, Y., Amari, S., & Pravdivtseva, O. 2002, ApJ, 575, 257
Loeffler, M. J., Baratta, G. A., Palumbo, M. E., Strazzulla, G., & Baragiola, R. A. 2005, A&A, 435, 587
Mennella, V., Palumbo, M. E., & Baratta, G. A. 2004, ApJ, 615, 1073
Nomura, H., & Millar, T. J. 2004, A&A, 414, 409
Nummelin, A., Whittet, D. C. B., Gibb, E. L., Gerakines, P. A., & Chiar, J. E. 2001, ApJ, 558, 185
Öberg, K. I., Fraser, H. J., Boogert, A. C. A., Bisschop, S. E., Fuchs, G. W., van Dishoeck, E. F., & Linnartz, H. 2007a, A&A, 462, 1187
Öberg, K. I., Fuchs, G. W., Awad, Z., Fraser, H. J., Schlemmer, S., van Dishoeck, E. F., & Linnartz, H. 2007b, ApJ, 662, L23
Öberg, K. I., Boogert, A. C. A., Pontoppidan, K. M., Blake, G. A., Evans, N. J., Lahuis, F., & van Dishoeck, E. F. 2008, ApJ, 678, 1032
Pontoppidan, K. M. 2006, A&A, 453, L47
Pontoppidan, K. M., Dartois, E., van Dishoeck, E. F., Thi, W.-F., & d'Hendecourt, L. 2003a, A&A, 404, L17
Pontoppidan, K. M., & Dullemond, C. P. 2005, A&A, 435, 595
Pontoppidan, K. M., et al. 2003b, A&A, 408, 981
Roser, J. E., Vidali, G., Manicò, G., & Pirronello, V. 2001, ApJ, 555, L61
Saraceno, P., Andre, P., Ceccarelli, C., Griffin, M., & Molinari, S. 1996, A&A, 309, 827
Shen, C. J., Greenberg, J. M., Schutte, W. A., & van Dishoeck, E. F. 2004, A&A, 415, 203
Shu, F. H. 1977, ApJ, 214, 488
Stantcheva, T., & Herbst, E. 2004, A&A, 423, 241
Tielens, A. G. G. M., & Hagen, W. 1982, A&A, 114, 245
Tielens, A. G. G. M., Tokunaga, A. T., Geballe, T. R., & Baas, F. 1991, ApJ, 381, 181
van Broekhuizen, F. A., Groot, I. M. N., Fraser, H. J., van Dishoeck, E. F., & Schlemmer, S. 2006, A&A, 451, 723
Whittet, D. C. B., Bode, M. F., Longmore, A. J., Adamson, A. J., McFadzean, A. D., Aitken, D. K., & Roche, P. F. 1988, MNRAS, 233, 321
Whittet, D. C. B., Shenoy, S. S., Bergin, E. A., Chiar, J. E., Gerakines, P. A., Gibb, E. L., Melnick, G. J., & Neufeld, D. A. 2007, ApJ, 655, 332
Whittet, D. C. B., et al. 1998, ApJ, 498, L159